



## Adaptive Droop Control for Voltage and Frequency Regulation in Virtual Power Plant under Power System Contingencies

Sindhura Gupta<sup>1\*</sup> , Susovan Mukhopadhyay<sup>2</sup> , Ambarnath Banerji<sup>3</sup> ,  
Prasun Sanki<sup>4</sup> , Sujit K. Biswas<sup>5</sup> 

<sup>1, 2, 4</sup> Department of Electrical Engineering, Netaji Subhash Engineering College, Kolkata, India  
E-mail: [sindhura.gupta@nsec.ac.in](mailto:sindhura.gupta@nsec.ac.in)

<sup>3</sup> Department of Electrical Engineering, Narula Institute of Technology, Kolkata, India

<sup>5</sup> Department of Electrical Engineering, St. Thomas' College of Engineering and Technology, Kolkata, India

Received: March 15, 2023

Revised: May 13, 2023

Accepted: May 22, 2023

**Abstract**—The frequent penetration of distributed energy resources in microgrid environment often faces operational challenges like stability and reliability issues. In order to overcome these challenges, the concept of the virtual power plant is suggested. Practically, the chance of voltage and frequency fluctuation increases in virtual power plant scenarios under critical power system contingencies like faults and sensitive load switching. Therefore, implementation of efficient controllers is required to address this issue. Further, the fixed gain droop control topology reported in literature is insufficient to accomplish seamless voltage and frequency regulation of the virtual power plants. Therefore, this paper proposes an adaptive droop control scheme to regulate system's frequency and voltage (as per IEEE 1547) in presence of critical power system contingencies under virtual power plant scenarios. Further, a small signal stability analysis is carried out considering the system Eigenvalues to investigate the effectiveness of the proposed adaptive droop controller. Additionally, a comparative analysis between traditional and proposed droop controller is performed considering critical power system contingencies under MATLAB / Simulink environment. The dynamic responses establish the improved performance of the proposed controller over the traditional control scheme in terms of transient and steady-state stability.

**Keywords**— Adaptive droop control; Distributed energy resource; Frequency regulation; Small signal stability; Virtual power plant; Voltage regulation; Power system contingency.

### NOMENCLATURE

$\omega_{act}, V_{act}$	Operating angular frequency in rad/s, operating voltage at PCC rms in volt	$\omega_{max}, \omega_{min}$	Upper and lower boundaries of angular frequency
$L_f, C_f$	Inductance in mh and capacitance in $\mu$ f of filter	$\Delta P, \Delta Q$	Mismatch in active and reactive power
$\omega_r, V_r$	Rated angular frequency in rad/s, rated voltage rms in volt	$V_{max}, V_{min}$	Upper and lower boundaries of voltage amplitude
$L_{cp}$	Coupling inductance in mh	$\omega_{c-f}$	Cut-off angular frequency of low pass filter in rad/s (power controller)
$P, Q$	Instantaneous active and reactive power in MW and MVAR	$I_{act}$	Operating current in ampere

$P_f, Q_f$	Maximum active and reactive power contribution from DER in MW and MVAR	$G_{ff}$	Feed-forward gain
$q, k$	Fixed frequency and voltage droop gain	$I_{fl-d}, I_{fl-q}$	LC filter dq-axis current component in ampere
$\Delta\omega, \Delta V$	Mismatch of angular frequency and voltage	$\delta_0$	Initial value of load angle in radian
$q_{er,n}, k_{eq,n}$	Adaptive frequency and voltage droop gain	$V_{bus-d}, V_{bus-q}$	dq-axis component of bus voltage in volt
$V_{ss-d}, V_{ss-q}$	Steady state initial operating voltage dq-axis component for LC filter in volt	$V_{in-d}, V_{in-q}$	dq-axis component of inverter voltage in volt
$I_{ss-d}, I_{ss-q}$	Steady state initial operating current dq-axis component for LC filter in ampere	$I'_{ss-d}, I'_{ss-q}$	Steady state initial operating current dq-axis component for coupling inductor in ampere
$K_{pv}, K_{iv}, K_{pi}, K_{il}$	The gain parameters of PI controller associated with outer voltage and inner current loop	$A_{mv}$	State matrix

## 1. INTRODUCTION

The concept of microgrid (MG) is extensively incorporated in modern power system scenarios to improve the overall system performance. MG can function either in islanded or in grid-connected mode operation. Generally, MG permits the frequent integration of local distributed energy resources (DERs), storage systems and different loads. In practical operation, the intermittent nature of DERs often hinders the balance between generated power and load-demanded power. Therefore, several operational challenges like frequency and voltage regulation, efficiency, reliability, and stability are common concerns in MG operation [1, 2]. In addition to that, MG application in large-scale power systems is limited due to the geographical availability and level of power generation from different DERs. Recently, the concept of a virtual power plant (VPP) has become very successful in order to address the above-discussed challenges raised in the MG scenario. VPP is capable to aggregate, manage and control various DERs together as a single entity. The participating DERs in the VPP scenario are not necessarily belonging to the same geographical location. Therefore, VPPs can be utilized as large-scale decentralized power systems. In practical application, inverters are often utilized in DER based VPPs in order to match load requirements. Therefore, proper control topology is required to regulate the voltage and frequency of DER-based inverters under various power system contingencies like faults and sensitive load switching. Additionally, small-signal stability analysis is essential to improve system dynamic characteristics. Till date, electricity market-related aspects in the VPP scenario are well addressed in several articles [3-6]. Although, very few articles have investigated operational challenges like voltage and frequency regulation and stability issues in order to evaluate the system performance of the VPP scenario.

Traditional DER based power systems are designed to function in grid-following mode (GFL) operation. The operation of DER based power systems in GFL mode blindly follow the grid frequency and voltage to contribute high quality power into the grid. Their operation totally depends upon the grid stability as they are unable to regulate grid frequency or

voltage. Therefore, these GFL-DER based power systems often face several operational challenges and stability issues. In this regard, recently the idea of grid-forming (GFM)-DER based power system has become very popular as they function independently even in the absence of grid stability. Additionally, GFL-DER based power systems with droop control topology provide seamless frequency and voltage regulation during transition from grid connected to islanded mode operation. It is noteworthy to mention that droop control is capable to ensure equal load sharing with minimum circulating current among the participating DERs. Additionally, the frequency and voltage oscillations during DER switching are limited by the droop control mechanism [7]. In this connection, an optimal droop control topology is suggested in [8] for DER-based systems in order to improve frequency regulation and system stability. However, the suggested control topology lacks detailed system modeling and voltage regulation issue. Additionally, controller designing is carried out only considering islanded mode operation. Further, Bintoudi et al. propose an agent-based droop control topology for DER based power system in [9]. In this article, an improved primary droop control topology is presented, which enables semi-centralized or distributed operation of DER based power system. However, less attention is given towards the detailed system modeling to evaluate system performance. Moreover, detailed discussion on frequency and voltage regulation of the suggested DER based power system is lacking in this article. Further, a distributed three-layer control topology is proposed in [10], where the power output of DERs is controlled to accomplish frequency regulation. Although, the suggested control scheme provides less priority towards the evaluation of system performance. Similarly, the frequency regulation of a DER-based power system is achieved by incorporating an optimal approach in [11]. However, voltage regulation and detailed system performance analysis under the suggested controller is lacking in the article. Unlike the above-discussed articles, the voltage regulation of islanded DER-based power systems is investigated using a distributed secondary control scheme in [12]. Accordingly, an improved sliding mode control scheme is suggested to control the operation of DER-based power system. However, the frequency regulation and system performance analysis are given less priority in the above-mentioned article. Similarly, Schiffer et al. propose a distributed reactive power control-based voltage regulation scheme for DER-based power systems [13]. In this article, less attention is given towards the frequency regulation issue while evaluating system performance. Recently, a neural network based secondary droop control scheme is suggested to control the voltage of islanded DER-based power system [14]. However, the frequency regulation of the suggested system is lacking in this article.

According to the detailed literature review, it is observed that most of the above-mentioned articles focus on the fixed droop gain control mechanism. The major bottleneck of the above-mentioned controller is its limited performance during power system critical contingencies like power system faults, induction motor switching and non-linear load switching. In this context, the concept of an adaptive droop control scheme is proposed where automatic droop gain adjustment is accomplished depending upon the magnitude of power system contingencies [15, 16]. However, the variation of droop coefficients due to contingencies causes frequency oscillations and voltage fluctuations. Therefore, system stability analysis is essential to ensure reliable operation for a DER-based VPP scenario along with frequency and voltage regulation. In this regard, the stability analysis of DER-based

power systems is carried out utilizing the root locus method [17]. The authors of the paper develop a small-signal model of a DER-based power system in order to investigate system stability. During the root locus analysis, it is observed that the low-frequency system Eigenvalues are very much sensitive to the stability of the considered DER-based power system. However, the complexity of the model limits its application in large-scale power systems. Furthermore, in [18, 19], droop controller gain parameter adjustment and equivalent line impedance values of DER-fed power systems are utilized to investigate system stability. However, in these articles, less attention is paid towards the system performance analysis during critical power system contingencies like faults, and sensitive load switching. Moreover, the droop gain variation is performed randomly instead of following any specific method in [18]. Therefore, improved particle swarm optimization (PSO) technique is incorporated to evaluate the droop control gain parameters in a DER-based power system in [20]. Although less attention is given towards detailed small-signal stability analysis while evaluating system performance.

Based on the critical literature survey, it is observed that available research works consider the voltage regulation, frequency regulation, controller designing and system stability analysis of DER-based power systems as separate issues. Additionally, less attention is paid towards controller performance evaluation during critical power system contingencies. In this context, it is noteworthy to mention that the time-scale of DER-based power systems varies within a few milliseconds [21]. Accordingly, the operating time constant of DER-based power systems are much faster than synchronous generator based power systems. Therefore, faster control topologies are required for DER-based power systems to regulate both operating frequency and voltage under different power system contingencies. This faster control approach, improves the dynamic performance of DER-based power systems in terms of active and reactive power sharing. Based on the above-discussed research gaps, this paper presents the following contributions.

This paper proposes an adaptive droop control scheme to accomplish seamless frequency and voltage regulation in GFM-DER based VPP system under different power system contingencies. The GFM mode operation with adaptive droop controller enables independent voltage and frequency regulation of the considered VPP system even in the absence of grid. The proposed control scheme is designed based on the popular active power versus frequency and reactive power versus voltage droop characteristics. Additionally, automatic adjustment of droop coefficients is designed depending upon the magnitude of a power system contingency.

Further, a small signal stability analysis considering DER-based inverter model is presented in order to investigate system performance. System Eigenvalues are evaluated to determine the operating ranges of the adaptive droop coefficients and the gain parameters of the PI controllers of the voltage and current loop to ensure stable system performances.

Additionally, PSO is incorporated to evaluate the optimal value of the PI controller gain parameters within the obtained range from the Eigenvalue analysis. In this regard, integral square error (ISE) based performance index is utilized to determine objective functions.

Finally, in this work, a comparative analysis between the adaptive droop control method and the traditional fixed gain droop control method is presented in order to establish better system performance under critical power system contingencies (like faults and different

load switching). It is noteworthy to mention that less than 1% frequency and 5% voltage regulation is obtained under the proposed controller during critical power system contingencies.

The rest of the paper is structured as follows. Section 2 represents the VPP configuration considered in this paper, followed by section 3 where detailed controller analysis is presented. In section 4, small-signal modeling for different parts of the controller is presented. Section 5 includes the Eigenvalue-based stability analysis. Next in section 6, simulation test results are presented with a detailed discussion. Finally, section 7 presents the concluding remarks.

## 2. SYSTEM CONFIGURATION

In practical operation, several DERs based on different renewable sources (like PV panels, wind generators, microturbines, and fuel cells) as well as Energy Storage Systems (ESS) are integrated into a VPP, which is capable to function as an independent power source. The traditional droop control topology can accomplish accurate sharing of power among participating DERs. In the traditional droop control method, frequency and voltage regulation is achieved using the fixed droop characteristics between active power-frequency ( $P$ - $f$ ) and reactive power-voltage ( $Q$ - $V$ ). However, the pre-specified droop characteristic of traditional droop control topology risk system stability under critical power system contingencies. Thus, additional restoration control during critical contingencies is required. In this context, often seamless control between the VPP internal units is carried out utilizing two-way communication channels. Therefore, transmission system operator (TSO) and distribution system operator (DSO) based supervisory load frequency control are necessary to manage the sudden contingencies [22]. However, such control topology prioritizes frequency regulation over voltage regulation to maintain power quality and system stability. In these circumstances, it is noteworthy to mention that frequency and voltage regulation are equally important to address the power quality and stability issues of VPP.

Therefore, this paper proposes an adaptive droop control topology to achieve seamless frequency and voltage regulation by dynamically adjusting the droop gain under critical power system contingencies. The proposed controller consists of three major loops-power controller, outer voltage control and inner current loop. The power controller regulates the frequency and voltage magnitude of inverters according to the dynamic adjustment of droop coefficients. Further, the outer voltage control loop is utilized to control voltage accurately. Additionally, the outer voltage control loop provides relevant inputs to the inner current loop. Finally, the inner current loop generates a reference voltage signal for pulse width modulation (PWM).

The proposed DER integrated VPP is depicted in Fig. 1. According to Fig. 1, each DER is connected to its base loads through three-phase inverters LC filters ( $L_f$  and  $C_f$  per phase respectively, and coupling inductors  $L_{cp}$ ). Further, the DER-driven inverter, filter, base load and coupling inductor are considered as a single unit. Likewise, a total of three units are considered to present the VPP model. In the considered VPP, individual units share common loads through the point of common coupling (PCC). Additionally, solid-state relay-driven static switches are incorporated at different stages in order to accomplish fast islanding operations under emergencies. The value of each parameter of the considered VPP model is included in Table 1.



where  $\omega_{act}$  and  $V_{act}$  are the system operating angular frequency (in rad/s) and point of common coupling voltage (in volt),  $\omega_r$  and  $V_r$  are the rated angular frequency (in rad/s) and voltage (in volt) of the system.  $P$  and  $Q$  are the instantaneous load active power (in MW) and reactive power (in MVAR) whereas  $P_f$  and  $Q_f$  are the maximum active power (in MW) and maximum reactive power (in MVAR) contribution from each DER. The term  $q$  and  $k$  represent the fixed frequency and voltage droop coefficients, as expressed by Eqs. (3) and (4).

$$q = \frac{(\omega_{act} - \omega_r)}{P_f} = \frac{\Delta\omega}{P_f} \quad (3)$$

$$k = \frac{(V_{act} - V_r)}{Q_f} = \frac{\Delta V}{Q_f} \quad (4)$$

where  $\Delta\omega$  and  $\Delta V$  represented the deviation of MG angular frequency with respect to the reference, due to change of load.

### 3.2. Adaptive Droop Control

The traditional fixed gain droop control scheme appears insufficient to regulate voltage and frequency while VPP is subjected to power system contingencies. In such scenario, this paper proposes an adaptive droop control topology to improve the overall frequency and voltage regulation by dynamically adjusting the droop coefficients depending on the magnitude of a power system contingency.

The proposed adaptive frequency and voltage droop gains  $q_{eq,n}$  and  $k_{eq,n}$  of  $n^{\text{th}}$  DER based inverter in VPP are evaluated as Eqs. (5) and (6):

$$q_{eq,n} = \begin{cases} \frac{\sqrt{(\omega_{act} - \omega_r)(\omega_{max} - \omega_{act})}}{|\Delta P|} & \text{when } (\omega_{act} - \omega_r) > 0 \\ \frac{\sqrt{(\omega_{act} - \omega_r)(\omega_{min} - \omega_{act})}}{|\Delta P|} & \text{when } (\omega_{act} - \omega_r) \leq 0 \end{cases} \quad (5)$$

$$k_{eq,n} = \begin{cases} \frac{\sqrt{(V_{act} - V_r)(V_{max} - V_{act})}}{|\Delta Q|} & \text{when } (V_{act} - V_r) > 0 \\ \frac{\sqrt{(V_{act} - V_r)(V_{min} - V_{act})}}{|\Delta Q|} & \text{when } (V_{act} - V_r) \leq 0 \end{cases} \quad (6)$$

Here,  $\omega_r$  and  $V_r$  represent the rated system angular frequency (in rad/s) and rated voltage (in volt) whereas  $\omega_{act}$  and  $V_{act}$  represent the operating angular frequency (in rad/s) and operating PCC voltage (in volt).  $\Delta P$  and  $\Delta Q$  represent the mismatch of active and reactive power between the present and the targeted value. In order to accomplish smooth, faster frequency and voltage regulation upper and lower boundary limits of angular frequency (rad/s) and voltage amplitude (volt) are considered as  $\omega_{max}, \omega_{min}, V_{max}, V_{min}$ .

Figs. 2(a) and (b) depict the dynamic nature of frequency and voltage regulation in an adaptive way when any disturbance takes place. In traditional droop control equations (according to Eqs. (3) and (4)) only the mismatch of angular frequency  $\Delta\omega$  and voltage  $\Delta V$  is considered to evaluate the droop coefficients  $q$  and  $k$ . Thus, the droop coefficients are

always constant under any load perturbation. However, in the proposed adaptive droop control scheme to avail the adjustable droop characteristics (according to Figs. 2(a) and (b)) apart from the mismatch of angular frequency  $\Delta\omega = (\omega_{act} - \omega_r)$  and voltage  $\Delta V = (V_{act} - V_r)$  the difference between the boundary limits with the operating values (i.e.  $(\omega_{max} - \omega_{act})$  for operating angular frequency over the rated value or  $(\omega_{min} - \omega_{act})$  for operating angular frequency lower the rated value, similarly  $(V_{max} - V_{act})$  for overvoltage and  $(V_{min} - V_{act})$  for under voltage) is also included. In addition to that, here in Eqs. (5) and (6), instead of considering the maximum active and reactive power capacity of each DER ( $P_f$  and  $Q_f$  according to Eqs. (3) and (4)), the modulus of mismatch of active power  $\Delta P$  (between the present and the targeted value) and reactive power  $\Delta Q$  (between the present and the targeted value) are considered. Thus, over-loading and under-loading both situations are considered.

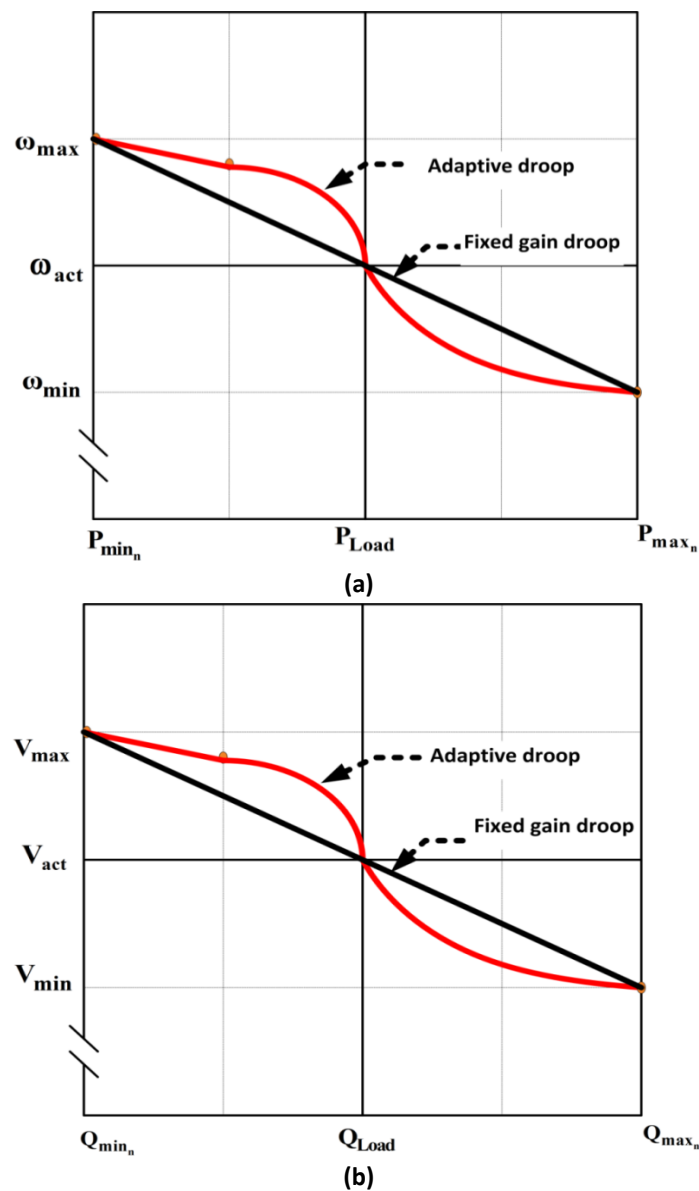


Fig. 2. Comparison between adaptive and traditional fixed gain methods: a) frequency droop control; b) voltage droop control.

Unlike the traditional approach (Eqs. (3) and (4)), this modification in numerator and denominator of Eqs. (5) and (6) helps to adjust the droop characteristic curves to a new operating point depending upon the magnitude of a power system contingency. Thus, when the mismatch of angular frequency and voltage is very small the inverter power controller's droop gains are comparatively less (as depicted in Figs. 2(a) and (b)). Accordingly, the inverter contributed power is also comparatively less. On the other hand, while this mismatch of frequency increases; the inverter's droop gain also increases resulting in increased inverter power output. Therefore, this adjustable relationship between the droop gain and inverter-contributed powers provides faster frequency and voltage regulation under different power system contingencies. As this flexible feature is not available in the traditional fixed gain droop controllers, regulation of frequency and voltage is comparatively more prolonged than this proposed one.

#### 4. SMALL SIGNAL MODELING

This section presents the small signal modeling of the considered VPP model (as depicted in Fig. 1). Primarily a single unit of VPP is considered to develop the small signal model. However, for n number of units, the same procedure is repeated. Generally, this analysis considers multiple non-linear equations. Further, these nonlinear equations are linearized around their operating points in order to accomplish stability analysis [25]. The step-by-step procedure to configure the model is presented in the following part.

##### 4.1. Adaptive Droop-Controlled Inverter and Interface Circuit

The major components of each DER are a three-phase voltage source inverter (VSI), LC filter and coupling inductor to interface with the common bus. Further, the adaptive droop controller of the VSI is divided into three sections (according to Fig. 1), power controller, outer voltage and inner current loop controller.

###### 4.1.1. Power Controller

The idea of this controller is to adjust the droop curve to a new operating point by dynamically adjusting the droop gains depending upon the magnitude of power system contingency (according to Figs. 2(a) and (b)). The basic block diagram of this controller is presented in Fig. 3. The instantaneous active power  $P$  (in MW) and the reactive power  $Q$  (in MVAR) are evaluated using the two-axis theory considering the output voltage and current (according to Eq. (7)).

$$\begin{cases} P = \frac{\omega_{c-f}}{s + \omega_{c-f}} (V_{act-d} I_{act-d} + V_{act-q} I_{act-q}) \\ Q = \frac{\omega_{c-f}}{s + \omega_{c-f}} (V_{act-d} I_{act-q} - V_{act-q} I_{act-d}) \end{cases} \quad (7)$$

A low pass filter is included here to filter out the high-frequency noise where  $\omega_{c-f}$  and  $s$  are the cut-off angular frequency (in rad/s) of the low pass filter and the factor of Laplace transform, respectively [26].  $V_{act-d}$ ,  $V_{act-q}$ ,  $I_{act-d}$  and  $I_{act-q}$  are the  $dq$  components of the operating voltages (in volt) and currents (in ampere). Now under small disturbance, Eq. (7) will be modified as Eq. (8):

$$\begin{cases} s\Delta P = \Delta\dot{P} = -\omega_{c-f}\Delta P + \omega_{c-f}(I'_{ss-d}\Delta V_{act-d} + I'_{ss-q}\Delta V_{act-q} + V_{ss-d}\Delta I_{act-d} + V_{ss-q}\Delta I_{act-q}) \\ s\Delta Q = \Delta\dot{Q} = -\omega_{c-f}\Delta Q + \omega_{c-f}(I'_{ss-d}\Delta V_{act-d} - I'_{ss-q}\Delta V_{act-q} - V_{ss-q}\Delta I_{act-d} + V_{ss-d}\Delta I_{act-q}) \end{cases} \quad (8)$$

where  $\Delta P$ ,  $\Delta Q$ ,  $\Delta V_{act-d}$ ,  $\Delta V_{act-q}$ ,  $\Delta I_{act-d}$  and  $\Delta I_{act-q}$  represent the small changes in active power, reactive power, operating voltage  $d$  component, operating voltage  $q$  component, operating current  $d$  component and operating current  $q$  component, respectively.  $V_{ss-q}$ ,  $V_{ss-d}$ ,  $I'_{ss-d}$  and  $I'_{ss-q}$  are the steady state operating points obtained after linearization. Considering the adaptive droop coefficients,  $\omega_{act}$  i.e., the angular frequency (in rad/s) and  $V_{act-d}^*$  and  $V_{act-q}^*$  (in volt) i.e., the voltage regulating equations can be presented as Eq. (9):

$$\begin{cases} \omega_{act} = \omega_r - q_{eq,n}(P - P_n) \\ V_{act-d}^* = V_r - k_{eq,n}(Q - Q_n) \\ V_{act-q}^* = 0 \end{cases} \quad (9)$$

where  $P_n$ ,  $Q_n$  are the maximum active power (in MW) and reactive power (in MVAR) capacities of  $n^{th}$  DER based unit. Further, for the realization of the small signal model, Eq. (9) is modified as Eq. (10):

$$\begin{cases} \Delta\omega = -q_{eq,n}\Delta P \\ \Delta V_{act-d}^* = -k_{eq,n}\Delta Q \\ \Delta V_{act-q}^* = 0 \end{cases} \quad (10)$$

Now, the angle difference between  $dq$  frames of individual inverters is converted in one common  $dq$  reference frame ( $\omega_x$ ) as represented in Eq. (11):

$$\delta = \int (\omega_{act} - \omega_x) dt \quad (11)$$

Further, for small signal disturbances Eq. (11) is simplified as Eq. (12):

$$\Delta\dot{\delta} = \Delta\omega - \Delta\omega_x = -q_{eq,n}\Delta P - \Delta\omega_x \quad (12)$$

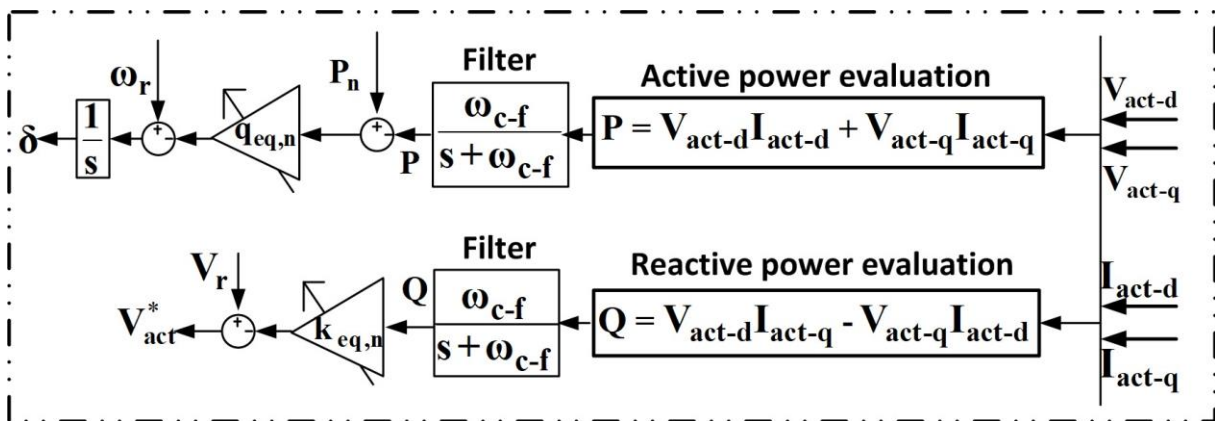


Fig. 3. Block diagram of the power controller.

#### 4.1.2. Outer Voltage Controller

Next in this section, a small signal model of typical outer voltage controller is presented as depicted in Fig. 4. It consists of a standard proportional integral regulator (PI) which compares the  $dq$  components of the actual output voltage  $V_{act-d}$  and  $V_{act-q}$  (in volt)

with reference values (obtained from the power controller)  $V_{act-d}^*$  and  $V_{act-q}^*$  (in volt) according to Fig. 3, to generate a voltage error signals. It also includes a feed-forward gain  $G_{ff}$  to handle the output current disturbances. The state space equations from outer voltage controller based on Fig. 4 are:

$$\begin{cases} \frac{d}{dt} \rho_d = \dot{\rho}_d = V_{act-d}^* - V_{act-d} \\ \frac{d}{dt} \rho_q = \dot{\rho}_q = V_{act-q}^* - V_{act-q} \end{cases} \quad (13)$$

$$\begin{cases} I_{fl-d}^* = \underbrace{K_{iv} \int \dot{\rho}_d + K_{pv}(V_{act-d}^* - V_{act-d})}_{PI} - \omega_r C_f V_{act-d} + G_{ff} I_{act-d} \\ = \underbrace{K_{iv} \rho_d + K_{pv}(V_{act-d}^* - V_{act-d})}_{PI} - \omega_r C_f V_{act-d} + G_{ff} I_{act-d} \\ I_{fl-q}^* = \underbrace{K_{iv} \int \dot{\rho}_q + K_{pv}(V_{act-q}^* - V_{act-q})}_{PI} + \omega_r C_f V_{act-q} + G_{ff} I_{act-q} \\ = \underbrace{K_{iv} \rho_q + K_{pv}(V_{act-q}^* - V_{act-q})}_{PI} + \omega_r C_f V_{act-q} + G_{ff} I_{act-q} \end{cases} \quad (14)$$

In Eq. (14), the proportional and integral gain parameters of the voltage controller attached PI regulator are presented as  $K_{pv}$  and  $K_{iv}$  respectively. Further, the small signal model realization of the considered voltage controller under small disturbances is presented as Eqs. (15) and (16) becomes:

$$\begin{cases} \Delta \dot{\rho}_d = \Delta V_{act-d}^* - \Delta V_{act-d} \\ \Delta \dot{\rho}_q = \Delta V_{act-q}^* - \Delta V_{act-q} \end{cases} \quad (15)$$

$$\begin{cases} \Delta I_{fl-d}^* = \underbrace{K_{iv} \int \Delta \dot{\rho}_d + K_{pv}(\Delta V_{act-d}^* - \Delta V_{act-d})}_{PI} - \omega_r C_f \Delta V_{act-d} + G_{ff} \Delta I_{act-d} \\ = \underbrace{K_{iv} \Delta \rho_d + K_{pv}(\Delta V_{act-d}^* - \Delta V_{act-d})}_{PI} - \omega_r C_f \Delta V_{act-d} + G_{ff} \Delta I_{act-d} \\ \Delta I_{fl-q}^* = \underbrace{K_{iv} \int \Delta \dot{\rho}_q + K_{pv}(\Delta V_{act-q}^* - \Delta V_{act-q})}_{PI} + \omega_r C_f \Delta V_{act-q} + G_{ff} \Delta I_{act-q} \\ = \underbrace{K_{iv} \Delta \rho_q + K_{pv}(\Delta V_{act-q}^* - \Delta V_{act-q})}_{PI} + \omega_r C_f \Delta V_{act-q} + G_{ff} \Delta I_{act-q} \end{cases} \quad (16)$$

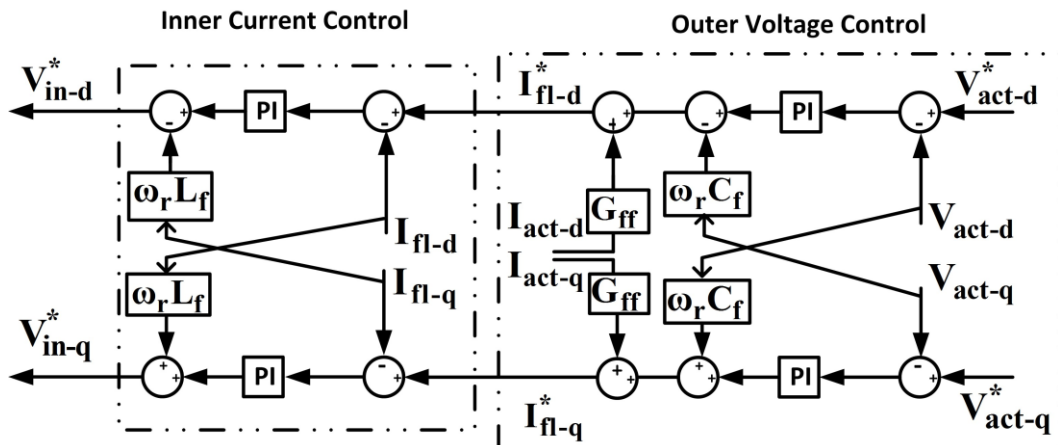


Fig. 4. Block diagram of inner current and outer voltage controller.

#### 4.1.3. Current Controller

Following the same procedure, the inner current controller is designed next. In this step, another PI controller is incorporated to compare the  $dq$  components of the filter current  $I_{fl-d}$  and  $I_{fl-q}$  (in ampere) with a reference (obtained at voltage controller output)  $I_{fl-d}^*$  and  $I_{fl-q}^*$  (in ampere) to generate the sinusoidal pulse width modulation (SPWM) signals  $V_{in-d}^*$  and  $V_{in-q}^*$  (in volt). The basic block diagram of this inner current controller is depicted in Fig. 4. The corresponding state space equation of the current controller loop is:

$$\begin{cases} \frac{d}{dt} \lambda_d = \dot{\lambda}_d = I_{fl-d}^* - I_{fl-d} \\ \frac{d}{dt} \lambda_q = \dot{\lambda}_q = I_{fl-q}^* - I_{fl-q} \end{cases} \quad (17)$$

$$\begin{cases} V_{in-d}^* = \underbrace{K_{il} \int \dot{\gamma}_d + K_{pl} (I_{fl-d}^* - I_{fl-d})}_{PI} - \omega_r L_f I_{fl-d} \\ = \underbrace{K_{il} \gamma_d + K_{pl} (I_{fl-d}^* - I_{fl-d})}_{PI} - \omega_r L_f I_{fl-d} \\ V_{in-q}^* = \underbrace{K_{il} \int \dot{\gamma}_q + K_{pl} (I_{fl-q}^* - I_{fl-q})}_{PI} + \omega_r L_f I_{fl-q} \\ = \underbrace{K_{il} \gamma_q + K_{pl} (I_{fl-q}^* - I_{fl-q})}_{PI} + \omega_r L_f I_{fl-q} \end{cases} \quad (18)$$

where  $\Delta \dot{\lambda}_d$  and  $\Delta \dot{\lambda}_q$  are the initial current errors which is fed to the PI controller to obtain Eq. (18). In order to realize the small signal model of the current control loop under small disturbances, Eqs. (17) and (18) are modified as Eqs. (19) and (20), respectively.

$$\begin{cases} \Delta \dot{\lambda}_d = \Delta I_{fl-d}^* - \Delta I_{fl-d} \\ \Delta \dot{\lambda}_q = \Delta I_{fl-q}^* - \Delta I_{fl-q} \end{cases} \quad (19)$$

$$\begin{cases} \Delta V_{in-d}^* = \underbrace{K_{il} \int \Delta \dot{\gamma}_d + K_{pl} (\Delta I_{fl-d}^* - \Delta I_{fl-d})}_{PI} - \omega_r L_f \Delta I_{fl-d} \\ = \underbrace{K_{il} \Delta \gamma_d + K_{pl} (\Delta I_{fl-d}^* - \Delta I_{fl-d})}_{PI} - \omega_r L_f \Delta I_{fl-d} \\ \Delta V_{in-q}^* = \underbrace{K_{il} \int \Delta \dot{\gamma}_q + K_{pl} (\Delta I_{fl-q}^* - \Delta I_{fl-q})}_{PI} + \omega_r L_f \Delta I_{fl-q} \\ = \underbrace{K_{il} \Delta \gamma_q + K_{pl} (\Delta I_{fl-q}^* - \Delta I_{fl-q})}_{PI} + \omega_r L_f \Delta I_{fl-q} \end{cases} \quad (20)$$

where  $K_{ip}$  and  $K_{il}$  are the proportional and integral gain parameters of the current controller attached PI regulator.  $I_{fl-d}$  and  $I_{fl-q}$  are the  $dq$  component of filter current (in ampere).

## 4.2. LC Filter and Coupling Inductance Models

The inverters are generally connected to the grid through LC ( $L_f$  in mH,  $C_f$  in  $\mu$ F) filter and coupling inductor  $L_{cp}$  (in mH) to reject the unwanted components of harmonics near switching frequency. Thus, the state space equations associated to LC filter with coupling inductor  $L_{cp}$  (based on Fig. 1) become:

$$\begin{cases} I_{fl-d}(R_f + sL_f) = L_f(\omega_{ss}I_{fl-q} + I_{ss-q}\omega) - (V_{in-d} - V_{act-d}) \\ I_{fl-q}(R_f + sL_f) = -L_f(\omega_{ss}I_{fl-d} + I_{ss-d}\omega) + (V_{in-q} - V_{act-q}) \end{cases} \quad (21)$$

$$\begin{cases} C_f \frac{d}{dt} V_{act-d} = C_f \dot{V}_{act-d} = (I_{fl-d} - I_{act-d}) + C_f(\omega_{ss}V_{act-q} + V_{ss-q}\omega) \\ C_f \frac{d}{dt} V_{act-q} = C_f \dot{V}_{act-q} = (I_{fl-q} - I_{act-q}) - C_f(\omega_{ss}V_{act-d} + V_{ss-d}\omega) \end{cases} \quad (22)$$

$$\begin{cases} I_{act-d}(R_{cp} + sL_{cp}) = (V_{act-d} - V_{bus-d}) + L_{cp}(\omega_{ss}I_{actl-q} + I'_{ss-q}\omega) \\ I_{act-q}(R_{cp} + sL_{cp}) = (V_{act-q} - \Delta V_{bus-q}) - L_{cp}(\omega_{ss}\Delta I_{actl-d} - I'_{ss-d}\Delta\omega) \end{cases} \quad (23)$$

After simplifying and rearranging Eqs. (21) and (23), we get Eqs. (24) and (25);

$$\begin{cases} \dot{I}_{fl-d} = -\frac{R_f}{L_f}I_{fl-d} + \omega_{ss}I_{fl-q} - \frac{1}{L_f}(V_{in-d} - V_{act-d}) + I_{ss-q}\omega \\ \dot{I}_{fl-q} = -\frac{R_f}{L_f}I_{fl-q} - \omega_{ss}I_{fl-d} + \frac{1}{L_f}(V_{in-q} - V_{act-q}) - I_{ss-d}\omega \end{cases} \quad (24)$$

$$\begin{cases} \dot{I}_{act-d} = \frac{1}{L_{cp}}(V_{act-d} - V_{bus-d}) + \omega_{ss}I_{actl-q} - \frac{R_{cp}}{L_{cp}}I_{act-d} + I'_{ss-q}\omega \\ \dot{I}_{act-q} = \frac{1}{L_{cp}}(V_{act-q} - V_{bus-q}) - \omega_{ss}I_{actl-d} - \frac{R_{cp}}{L_{cp}}I_{act-q} - I'_{ss-d}\omega \end{cases} \quad (25)$$

Further, under small disturbance, Eqs. (22), (24) and (25) modified as Eqs. (26), (27) and (28):

$$\begin{cases} \Delta \dot{I}_{fl-d} = -\frac{R_f}{L_f}\Delta I_{fl-d} + \omega_{ss}\Delta I_{fl-q} - \frac{1}{L_f}(\Delta V_{in-d} - \Delta V_{act-d}) + I_{ss-q}\Delta\omega \\ \Delta \dot{I}_{fl-q} = -\frac{R_f}{L_f}\Delta I_{fl-q} - \omega_{ss}\Delta I_{fl-d} + \frac{1}{L_f}(\Delta V_{in-q} - \Delta V_{act-q}) - I_{ss-d}\Delta\omega \end{cases} \quad (26)$$

$$\begin{cases} \Delta \dot{I}_{act-d} = \frac{1}{L_{cp}}(\Delta V_{act-d} - \Delta V_{bus-d}) + \omega_{ss}\Delta I_{actl-q} - \frac{R_{cp}}{L_{cp}}\Delta I_{act-d} + I'_{ss-q}\Delta\omega \\ \Delta \dot{I}_{act-q} = \frac{1}{L_{cp}}(\Delta V_{act-q} - \Delta V_{bus-q}) - \omega_{ss}\Delta I_{actl-d} - \frac{R_{cp}}{L_{cp}}\Delta I_{act-q} - I'_{ss-d}\Delta\omega \end{cases} \quad (27)$$

$$\begin{cases} \Delta \dot{V}_{act-d} = \frac{1}{C_f}(\Delta I_{fl-d} - \Delta I_{act-d}) + \omega_{ss}\Delta V_{act-q} + V_{ss-q}\Delta\omega \\ \Delta \dot{V}_{act-q} = \frac{1}{C_f}(\Delta I_{fl-q} - \Delta I_{act-q}) - \omega_{ss}\Delta V_{act-d} - V_{ss-d}\Delta\omega \end{cases} \quad (28)$$

Here the  $dq$  components of the bus voltage (in volt) are represented as  $V_{bus-d}$  and  $V_{bus-q}$ .  $V_{in-d}$  and  $V_{in-q}$  are the  $dq$  components of the inverter voltage (in volt).  $\omega_{ss}$ ,  $I_{ss-d}$ ,  $I_{ss-q}$  are the steady state  $dq$  components of initial values of all the operating points. The values of all steady state initial operating points are furnished in Table 2.

### 4.3. Complete Small-Signal Model

Finally, combining all above mentioned controller state space equations, the complete small signal model of one DER based unit can be presented in matrix format considering total 13 states. The output  $I_{act-dq}^c$  and input  $V_{bus-dq}^c$  are converted in common  $dq$  frame as:

$$[I_{act-dq}^c] = [F][I_{act-dq}] = \begin{bmatrix} \cos \delta & -\sin \delta \\ \sin \delta & \cos \delta \end{bmatrix} [I_{act-dq}] \quad (29)$$

$$[V_{bus-dq}] = [F^{-1}][V_{bus-dq}^c] = \begin{bmatrix} \cos \delta & \sin \delta \\ -\sin \delta & \cos \delta \end{bmatrix} [V_{bus-dq}^c] \quad (30)$$

Further, under small disturbance, Eqs. (31) and (32) are obtained after linearizing Eqs. (29) and (30):

$$[\Delta I_{act-dq}^c] = \begin{bmatrix} \cos \delta_0 & -\sin \delta_0 \\ \sin \delta_0 & \cos \delta_0 \end{bmatrix} [\Delta I_{act-dq}] + \begin{bmatrix} -I'_{ss-d} \sin \delta_0 - I'_{ss-q} \cos \delta_0 \\ I'_{ss-q} \cos \delta_0 - I'_{ss-d} \sin \delta_0 \end{bmatrix} [\Delta \delta] \quad (31)$$

$$[\Delta V_{bus-dq}] = \begin{bmatrix} \cos \delta_0 & \sin \delta_0 \\ -\sin \delta_0 & \cos \delta_0 \end{bmatrix} [\Delta V_{bus-dq}^c] + \begin{bmatrix} -V_{bus-d}^c \sin \delta_0 + V_{bus-q}^c \cos \delta_0 \\ V_{bus-d}^c \cos \delta_0 - V_{bus-q}^c \sin \delta_0 \end{bmatrix} [\Delta \delta] \quad (32)$$

Here,  $\delta_0$  considered as steady state load angle (in radian). Finally, the standard input output state space equations of n number of DER fed inverter models is presented as:

$$[\dot{\Delta x}_{inv-n}] = A_{inv-n} [\Delta x_{inv-n}] + B_{inv-n} [\Delta V_{bus-dq-n}^c] + B_{n-\omega_x} [\Delta \omega_x] \quad (33)$$

where,

$$[\Delta x_{inv-n}] = [\Delta \delta_n \quad \Delta P_n \quad \Delta Q_n \quad \Delta \rho_{d-n} \quad \Delta \rho_{q-n} \quad \Delta \lambda_{d-n} \quad \Delta \lambda_{q-n} \quad \Delta I_{fl-d-n} \quad \Delta I_{fl-q-n} \quad \Delta V_{act-d-n} \quad \Delta V_{act-q-n} \quad \Delta I_{act-d-n} \quad \Delta I_{act-q-n}]^T \quad (34)$$

$$\begin{bmatrix} \Delta \omega_n \\ \Delta I_{act-dq-n}^c \end{bmatrix} = \begin{bmatrix} C_{inv-\omega-n} \\ C_{inv-c-n} \end{bmatrix} [\Delta x_{inv-n}] \quad (35)$$

$$A_{inv-1} =$$

$$\begin{bmatrix} 0 & -q_{eq,n} & 0 & 0 & 0 & 0 & 0 & 0 & 0 & 0 & 0 & 0 & 0 & 0 \\ 0 & -\omega_{c-f} & 0 & 0 & 0 & 0 & 0 & 0 & 0 & \omega_{c-f} I'_{ss-d} & \omega_{c-f} I'_{ss-q} & \omega_{c-f} V_{ss-d} & \omega_{c-f} V_{ss-d} \\ 0 & 0 & -\omega_{c-f} & 0 & 0 & 0 & 0 & 0 & 0 & \omega_{c-f} I'_{ss-q} & -\omega_{c-f} I'_{ss-d} & -\omega_{c-f} V_{ss-q} & \omega_{c-f} V_{ss-q} \\ 0 & 0 & -k_{eq,n} & 0 & 0 & 0 & 0 & 0 & 0 & -1 & 0 & 0 & 0 \\ 0 & 0 & 0 & 0 & 0 & 0 & 0 & 0 & 0 & 0 & -1 & 0 & 0 \\ 0 & 0 & -k_{eq,n} K_{pv} & K_{iv} & 0 & 0 & 0 & -1 & 0 & -K_{pv} & -\omega_r C_f & G_{ff} & 0 \\ 0 & 0 & 0 & 0 & K_{iv} & 0 & 0 & 0 & -1 & \omega_r C_f & -K_{pv} & 0 & G_{ff} \\ 0 & -q_{eq,n} I_{ss-d} & \frac{k_{eq,n} K_{pv} K_{pl}}{L_f} & \frac{K_{iv} K_{pl}}{L_f} & 0 & \frac{K_{il}}{L_f} & 0 & \frac{-K_{pl} - R_f}{L_f} & \omega_{ss} - \omega_r & \frac{-K_{pv} K_{pl} - 1}{L_f} & \frac{\omega_r C_f K_{pl}}{L_f} & \frac{K_{pl} G_{ff}}{L_f} & 0 \\ 0 & q_{eq,n} I_{ss-q} & 0 & 0 & \frac{K_{iv} K_{pl}}{L_f} & 0 & \frac{K_{il}}{L_f} & \omega_{ss} - \omega_r & \frac{-K_{pl} - R_f}{L_f} & \frac{\omega_r C_f K_{pl}}{L_f} & \frac{-K_{pv} K_{pl} - 1}{L_f} & 0 & \frac{K_{pl} G_{ff}}{L_f} \\ 0 & -q_{eq,n} V_{act-q} & 0 & 0 & 0 & 0 & 0 & \frac{1}{C_f} & 0 & 0 & \omega_{ss} & -\frac{1}{C_f} & 0 \\ 0 & q_{eq,n} V_{act-d} & 0 & 0 & 0 & 0 & 0 & 0 & \frac{1}{C_f} & -\omega_{ss} & 0 & 0 & -\frac{1}{C_f} \\ \frac{x}{L_{cp}} & -q_{eq,n} I'_{ss-d} & 0 & 0 & 0 & 0 & 0 & 0 & 0 & \frac{1}{L_{cp}} & 0 & -\frac{R_{cp}}{L_{cp}} & \omega_{ss} \\ \frac{y}{L_{cp}} & q_{eq,n} I'_{ss-q} & 0 & 0 & 0 & 0 & 0 & 0 & 0 & 0 & \frac{1}{L_{cp}} & -\omega_{ss} & -\frac{R_{cp}}{L_{cp}} \end{bmatrix} \quad (36)$$

where  $x = V_{bus-d}^c \sin \delta_0 - V_{bus-q}^c \cos \delta_0$ ,  $y = V_{bus-d}^c \cos \delta_0 + V_{bus-q}^c \sin \delta_0$

Table 2. Initial values of Unit-1 operating parameters in VPP.

Parameter	Value	Parameter	Value	Parameter	Value
Steady state voltage $d$ -axis component for LC filter $V_{ss-d}$	311.5 V	Steady state current $d$ -axis component for LC filter $I_{ss-d}$	30.95 A	Bus voltage $d$ -axis component $V_{bus-q}$	-3 V
Steady state voltage $q$ -axis component for LC filter $V_{ss-q}$	0 V	Steady state current $q$ -axis component for LC filter $I_{ss-q}$	-10.05 A	Instantaneous active power $P$	80 MW
Steady state current $d$ -axis component for $L_{cp}$ $I'_{ss-d}$	30.95 A	Steady state angular frequency $\omega_{ss}$	314 rad/s	Instantaneous reactive power $Q$	60 MVAR
Steady state current $q$ -axis component for $L_{cp}$ $I'_{ss-q}$	-0.2 A	Bus voltage $q$ -axis component $V_{bus-d}$	308.7 V	Initial load angle $\delta_0$	0.22e-3 rad

### 5. STABILITY ANALYSIS USING EIGENVALUE

Further, in this section, detailed stability analysis (of a single unit under considered VPP) based on the obtained small signal model is carried out utilizing Eigenvalue spectrum as depicted in Fig. 5. In this regard, the elements of the state matrix  $A_{inv-1}$  are calculated considering the initial values of each parameter.

According to Fig. 5, it is observed that the Eigenvalues are scattered in the three different sections on the left-hand side of the real-imaginary plot. Moreover, it is evident that Eigenvalues which reside nearer to origin (dominant Eigenvalue) are very much sensitive in terms of system dynamics. Further, these dominant Eigenvalues are responsible for high system oscillations [27].

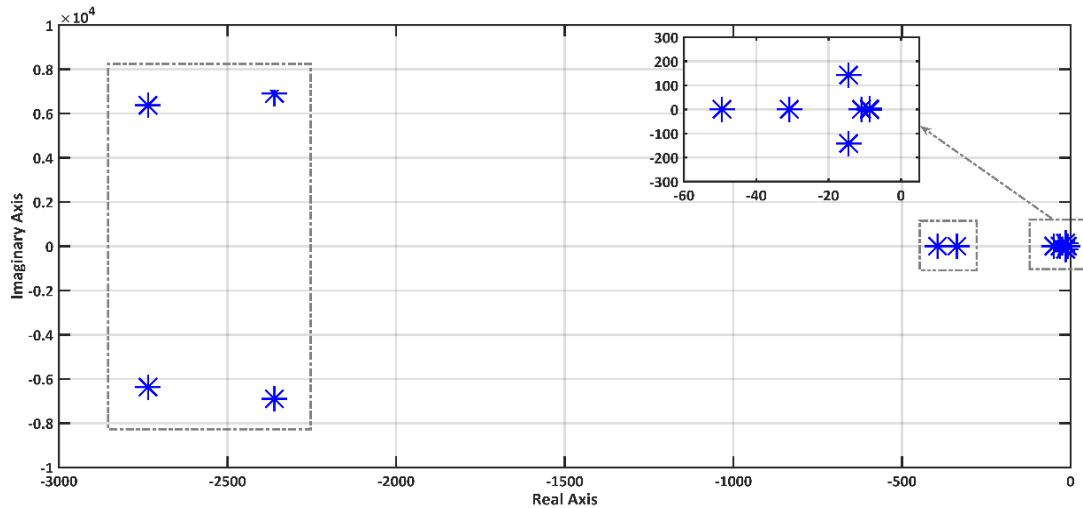


Fig. 5. Eigenvalues of Unit-1 state matrix.

The range of adaptive frequency and voltage coefficients ( $q_{eq,n}$  and  $k_{eq}$ ) are at first evaluated by testing the VPP model under critical power system contingencies in MATLAB/Simulink environment (Figs. 6(a) and (b)). The obtained range of the coefficients is validated using Eigenvalue analysis as presented in Figs. 6(c) and (d) where, the displacement of dominating Eigenvalues is minimal.

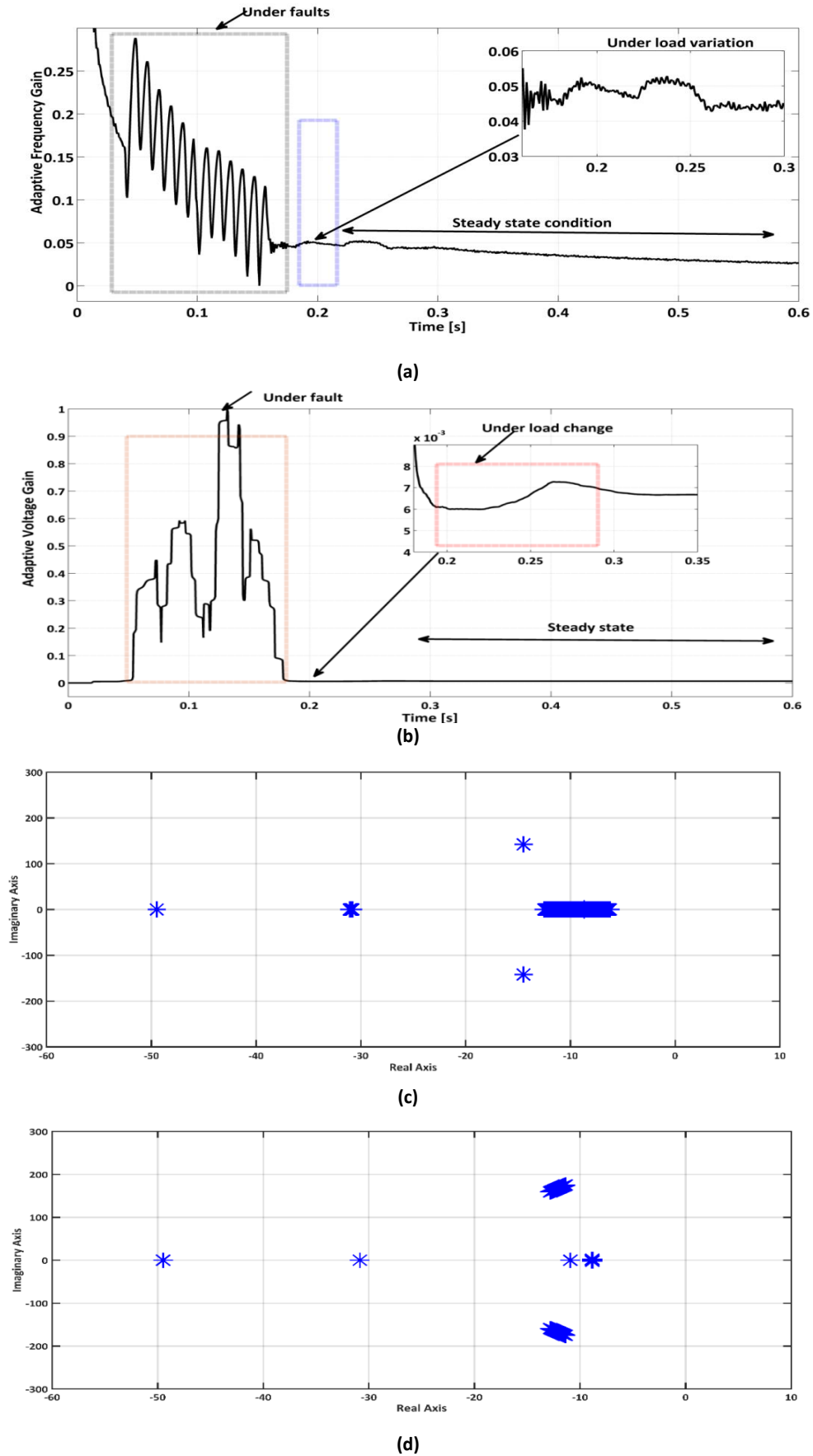


Fig. 6. a) Adaptive frequency droop gain adjustment; b) adaptive voltage droop gain adjustment under power system contingencies; c) dominant root locus as  $q_{eq} \in [0.004, 0.4]$ ; d) dominant root locus as  $k_{eq} \in [0.00005, 0.9]$ .

Additionally, the PI controller gain parameters of voltage and current loop play an important role in system dynamics. Thus, the gain parameters of these PI controllers are selected in two steps.

Firstly, a range of gain parameters ( $K_{pv}$ ,  $K_{iv}$ ,  $K_{pi}$  and  $K_{il}$ ) are obtained from Eigenvalue analysis in order to ensure stable system response (assuring all Eigenvalues situated left-hand side of the s-plane) as depicted in Figs. 7 and 8. Next, the optimal values of the PI controller gain parameters are evaluated from its respective selected ranges to assure an improved transient and steady state response. In this connection, integral square error (ISE) technique is incorporated to determine the minimum objective function [28] in presence of PSO algorithm as presented in Eq. (37).

$$\text{Min } \Gamma_{ISE} = \int_0^T [\alpha(\omega_r - \omega_{act})^2 + \beta(V_r - V_{act})^2] dt \tag{37}$$

Subjected to:

$$\left. \begin{aligned} K_{pv-MAX} < K_{pv} < K_{pv-MIN} \\ K_{iv-MAX} < K_{iv} < K_{iv-MIN} \\ K_{pi-MAX} < K_{pi} < K_{pi-MIN} \\ K_{il-MAX} < K_{il} < K_{il-MIN} \end{aligned} \right\} \tag{38}$$

Here,  $T$  presents the simulation time,  $\alpha$  and  $\beta$  presents the weightage factors.

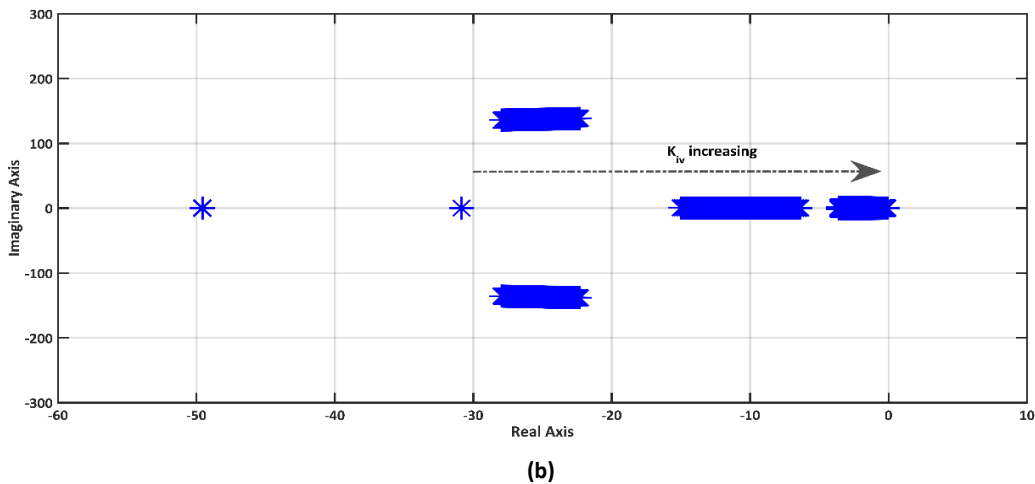
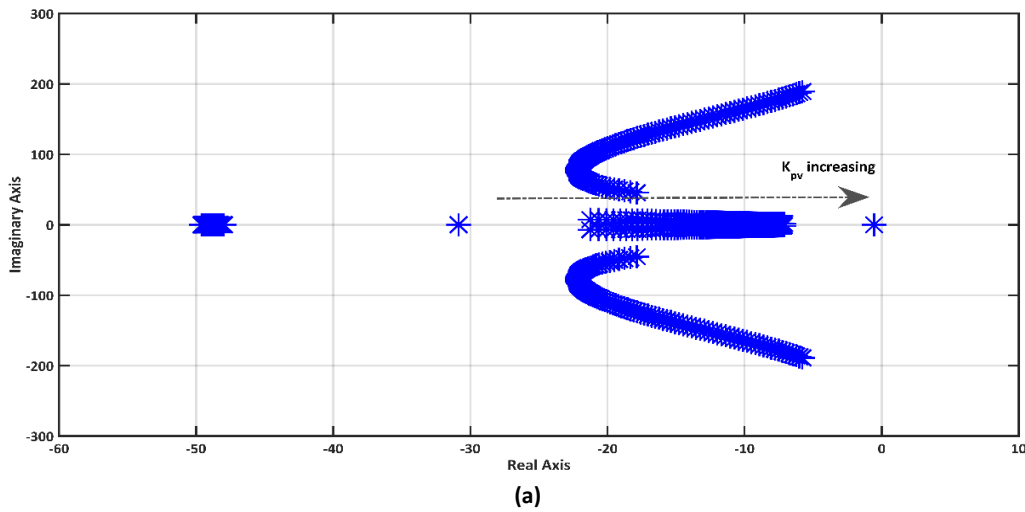


Fig. 7. a) Variation of dominant Eigenvalue for  $K_{pv} \in [1, 100]$ ; b) variation of dominant Eigenvalue  $K_{iv} \in [0.1, 50]$ .

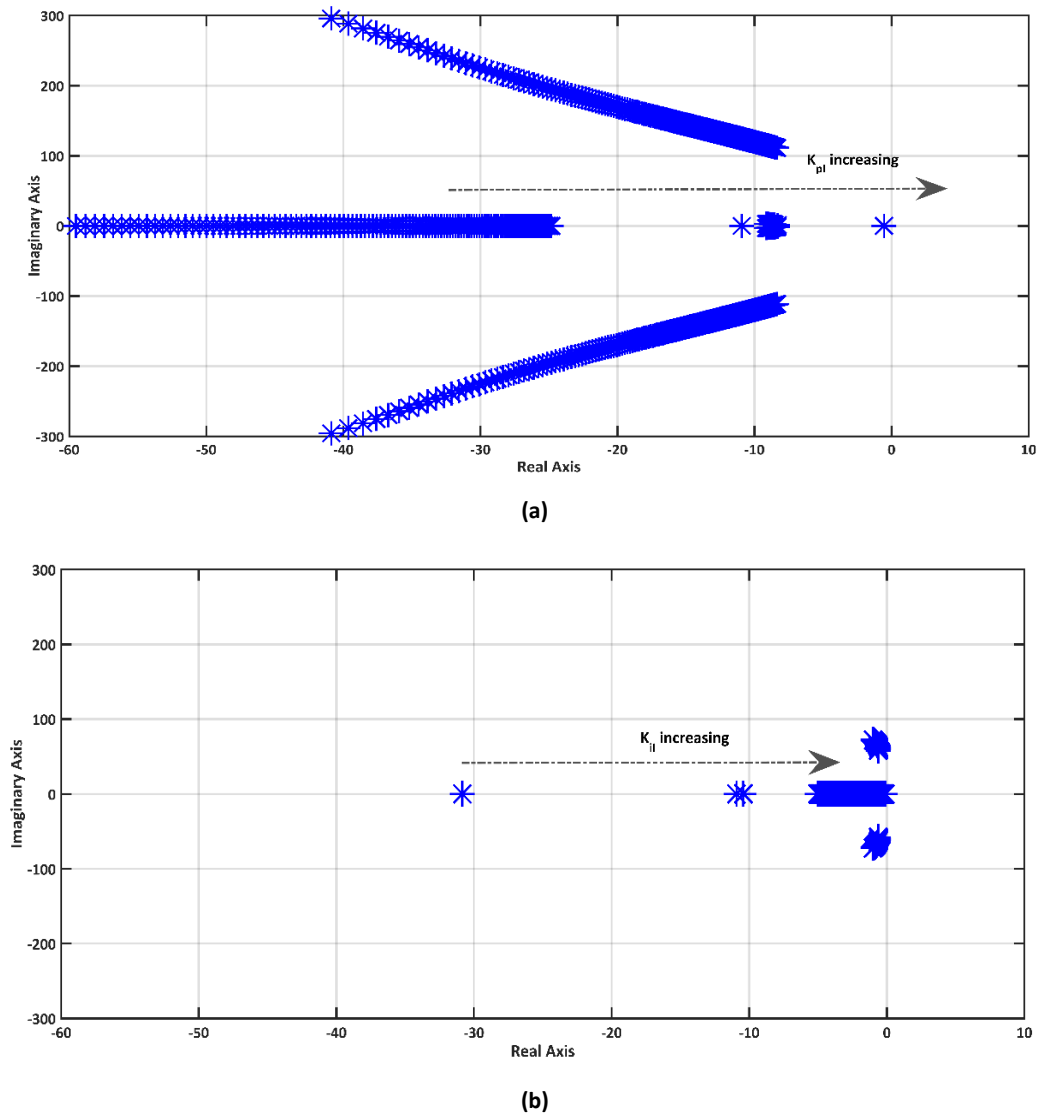


Fig. 8. a) Variation of dominant Eigenvalue  $K_{pi} \in [1, 100]$ ; b) variation of dominant Eigenvalue  $K_{II} \in [0.1, 50]$ .

## 6. SIMULATION RESULTS AND DISCUSSION

Power systems often experience small or large frequency and voltage fluctuations under different contingencies. Thus, this section presents the detailed simulation results of different power system contingencies both inside and outside of the VPP to validate the effectiveness of the proposed controllers. As discussed earlier the considered VPP is modeled considering three DER fed units (represented as Unit-1, Unit-2 and Unit-3). In this considered VPP model, different types of faults and load perturbations are tested utilizing both traditional droop control and adaptive droop control topology. Accordingly, a conventional droop control topology [29] is considered to develop the comparative analysis between fixed gain droop control and proposed adaptive droop control method. The comparative results of each test case are demonstrated in the following section to establish the improved transient and steady state response of the proposed adaptive controller over the traditional droop controller in terms of frequency and voltage regulation under critical power system contingencies. The brief overview of simulation case studies is depicted in Fig. 9.

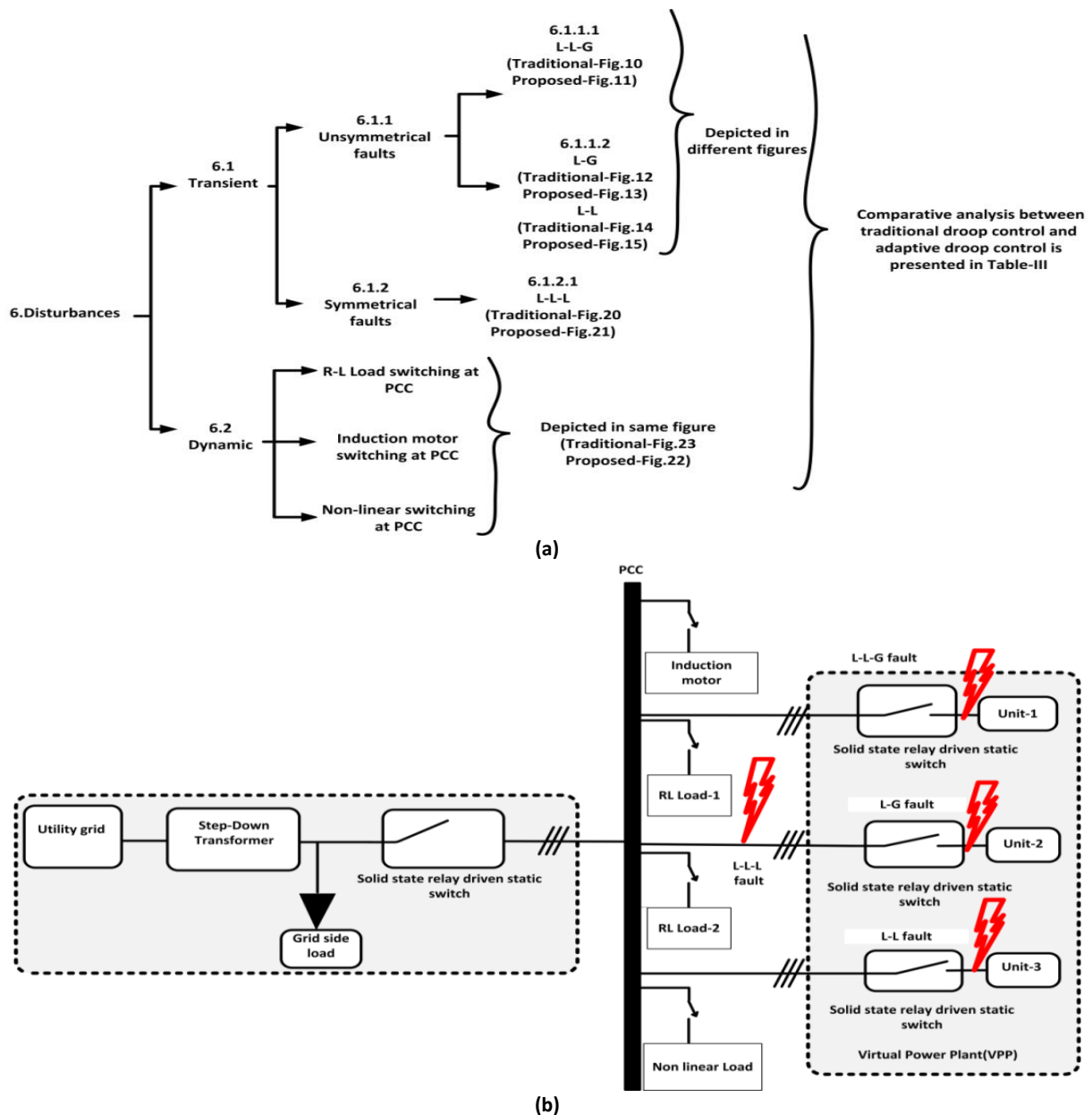


Fig. 9. a) Overview of simulation tests in VPP; b) location of different load switching and fault locations of VPP.

### 6.1. Performance Analysis during Large Magnitude Contingencies using Adaptive Droop Control Topology and Traditional Droop Control Method

Power system currents do not only become abnormally high during faults but also spread very fast amongst the connected components. Normally, when a fault occurs in the utility grid or in VPP system, temporary isolation of the faulted portion is carried out utilizing relay circuit breaker combination to interrupt the fast propagation of fault current. Further, after fault clearance reconnection of VPP with utility grid resumes, enabling interconnected operation. In this work, the suggested VPP model is tested with different symmetrical and unsymmetrical faults in MATLAB/Simulink environment under the proposed adaptive droop control topology. Further, a comparative analysis between tradition and proposed adaptive droop control scheme under different fault situations is presented to highlight the improved transient performance in terms of frequency and voltage regulation.

### 6.1.1. Unsymmetrical Faults

Unsymmetrical faults in transmission or in distribution lines cause unequal phase shifts in three-phase voltage and current. Additionally, current rises abnormally during faults as very low impedance is offered by the fault location. Under such condition, relay circuit breaker together identifies and isolates the fault-affected sections in order to restrict the propagation of the fault current. Thus, the interval between fault initiations to fault clearance is very crucial for the DER-based VPP scenario to sustain the impact of fault current. In this connection, the proposed controller attempts to regulate the frequency below 1% and voltage below 5% during this crucial interval. Accordingly, the considered VPP model is intentionally tested with unsymmetrical faults like line-to-line-to-ground (L-L-G), line-to-line (L-L) and line-to-ground (L-G) at different instants of the simulation run time to establish the improved performance of the proposed droop control method over the traditional droop control method.

- L-L-G Fault:** According to Fig. 9(b) at first, the VPP simulation model is tested under L-L-G fault at the instant of 0.03 s. The fault is created inside Unit-1 of the considered VPP. When the fault takes place, temporary isolation of Unit-1 is carried out by the associated solid-state relay-driven static switch (functions like relay and circuit breaker) in order to restrict the propagation of fault current from the remaining power system. Thus, Unit-1 operates as islanded part till clearance of the fault i.e. 0.09 s. In this situation, Figs. 10(a), 10(b), 11(a), and 11(b) depict the performance of traditional and proposed adaptive droop control topology in terms of frequency and voltage regulation.

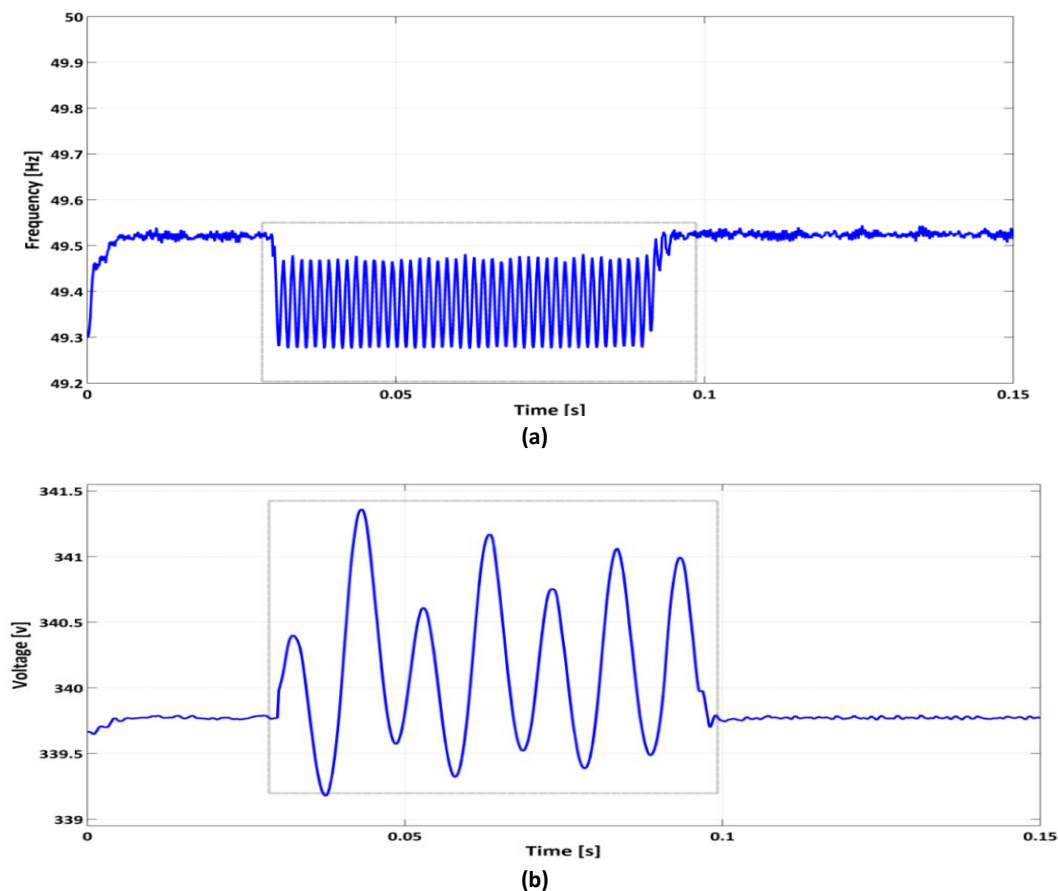


Fig. 10. a) Operating frequency; b) operating voltage of traditional droop control based Unit-1 under L-L-G fault.

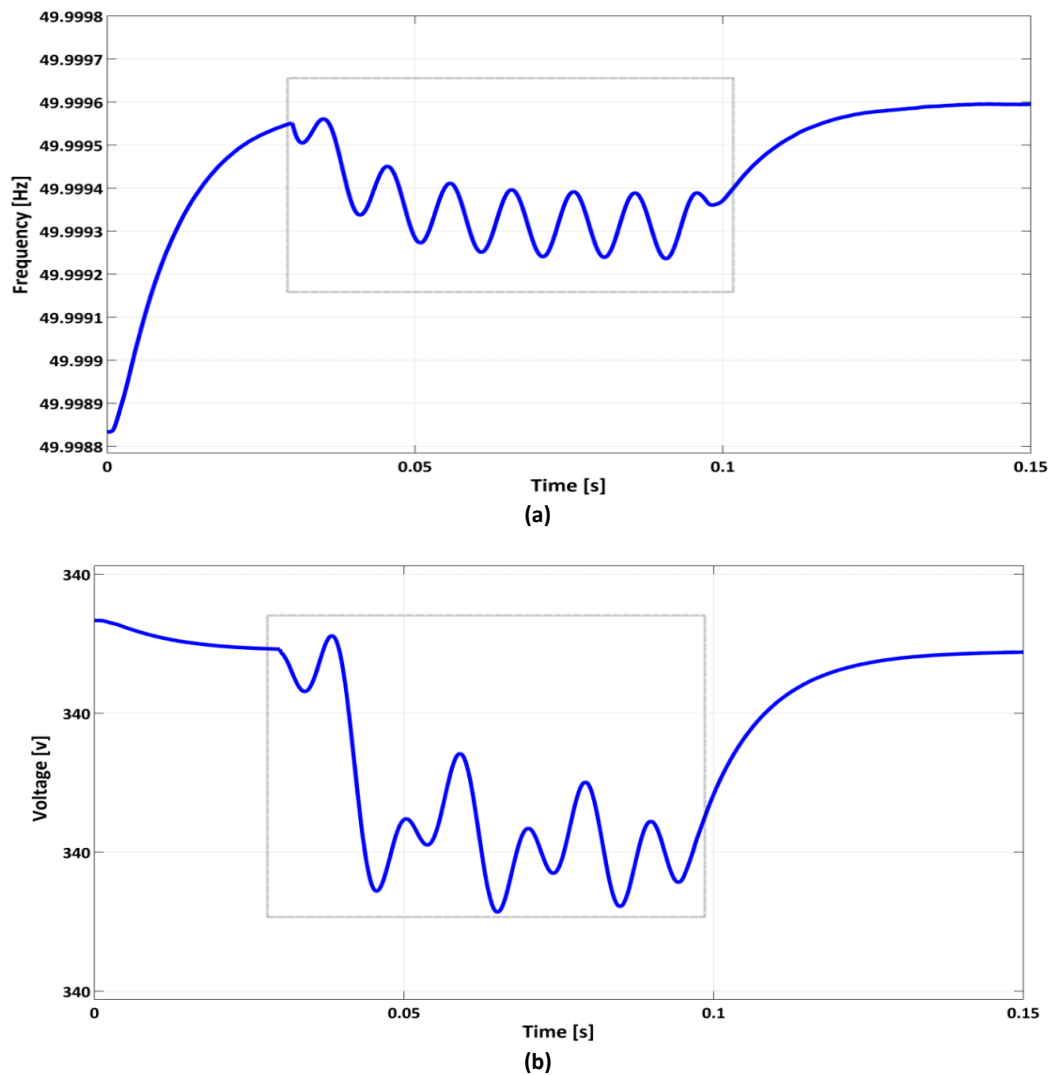


Fig. 11. a) Operating frequency; b) operating voltage of adaptive droop control based Unit-1 under L-L-G fault.

According to Figs. 10(a) and (b), in case of a traditional droop controller (the highlighted area inside the box), the frequency and voltage oscillation sustains (between the range of 49.0-49.5 Hz for frequency and 339.999-340.0013 V for voltage) till the fault clearance. However, in case of the proposed adaptive droop control method, due to the dynamic adjustment of frequency and voltage droop coefficients, fluctuation of frequency and voltage is significantly less (according to Figs. 11(a) and (b)). It is clearly visible in Figs. 11(a) and (b) that the proposed controller regulates frequency between the range of 49.9992-49.9994 Hz and voltage very close to 340 V even under the fault situation.

- L-G and L-L Fault:** Next, other two unsymmetrical faults L-G and L-L faults are tested in Unit-2 and in Unit-3 respectively as depicted in Fig. 9(b). Like the previous case, solid state relay driven static switches perform selective isolation of the fault locations. Thus, at 0.08 s Unit-2 (for the L-G fault) and at 0.1 s Unit-3 (for the L-L fault) are islanded to restrict the propagation of fault currents. The performance of traditional and proposed adaptive droop controller during these fault scenarios is presented between Figs. 12 to 15, where Figs. 12(a) and (b) depicts the Unit-2 frequency and voltage responses while regulated by traditional droop controller under L-G fault case.

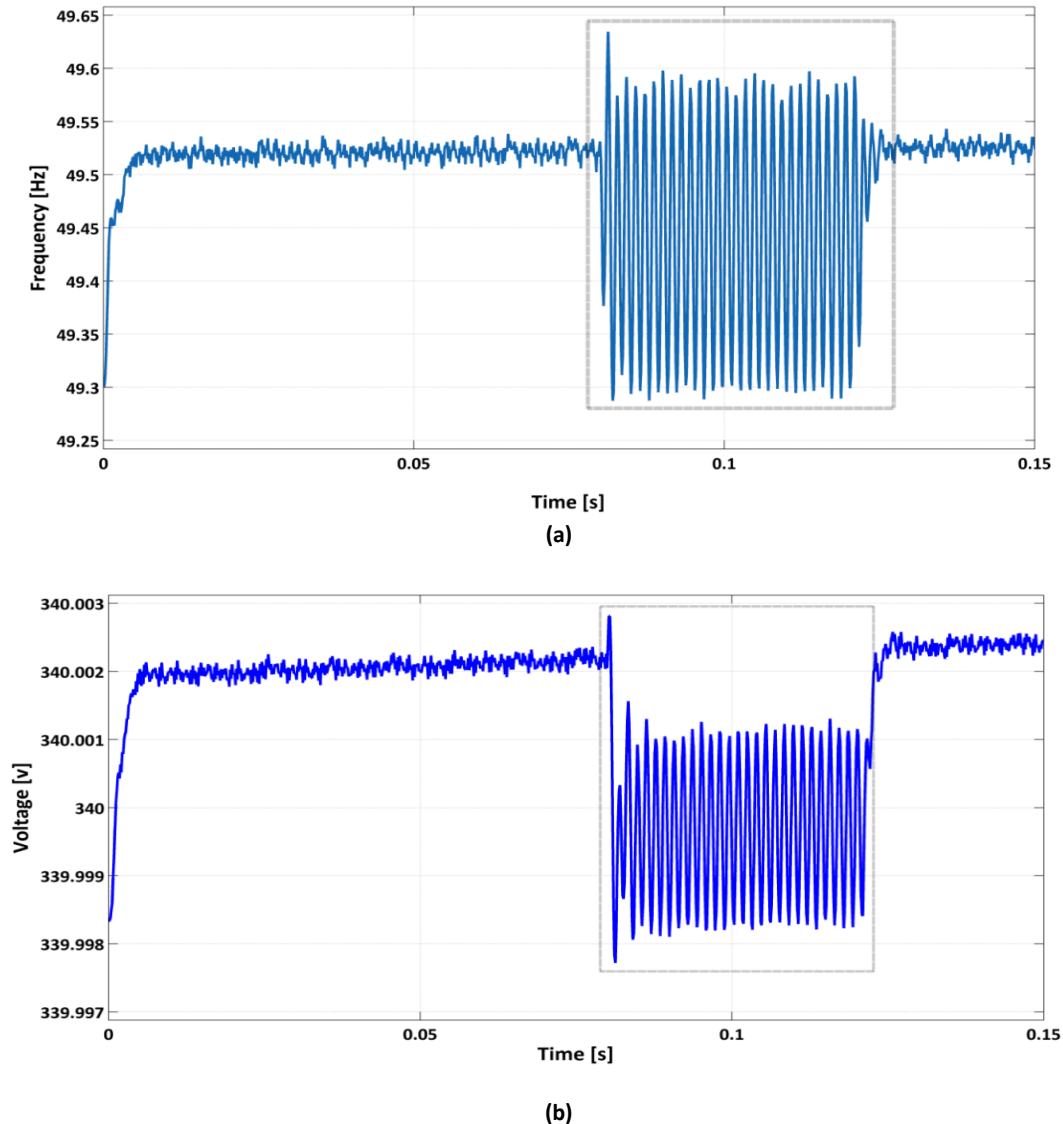
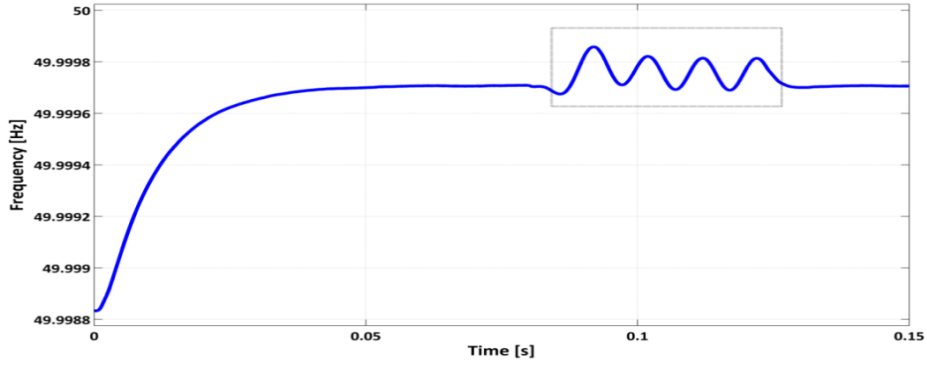


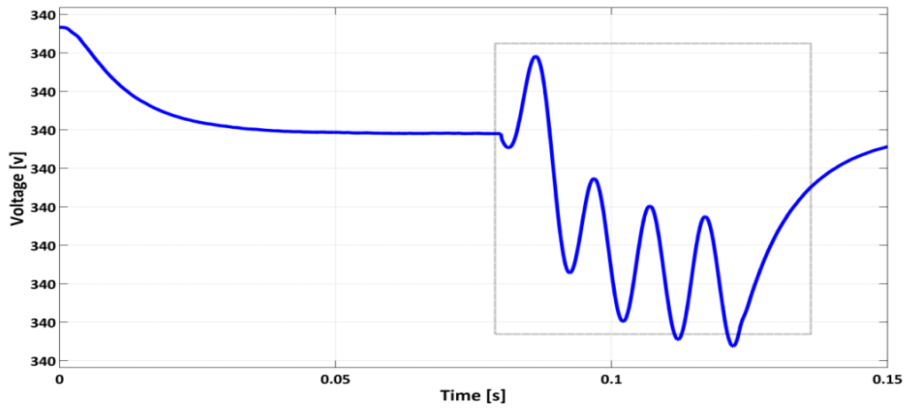
Fig. 12. a) Operating frequency; b) operating voltage of traditional droop control based Unit-2 under L-G fault.

Similarly, Figs. 13(a) and (b) present the Unit-2 frequency and voltage responses while regulated by the proposed adaptive droop controller under the L-G fault case. Further, Figs. 14(a) and (b) depict the Unit-3 frequency and voltage responses while regulated by a traditional droop controller under an L-L fault. Finally, Figs. 15(a) and (b) presents the Unit-3 frequency and voltage responses while regulated by an adaptive droop controller under an L-L fault.

Based on Figs. 12, 13, 14, and 15, it can be stated that the oscillation of voltage and frequency around their respective nominal value is significantly less in case of the proposed adaptive droop control under the fault situations. Further, the selective isolation of the fault-affected units under considered VPP restricts the propagation of fault current in the remaining power system. In this situation, the three-phase voltage and current waveforms of the individual units (Figs. 16(a) and (b) for Unit-1 output voltage and current, Figs. 17(a) and (b) for Unit-2 output voltage and current, and Figs. 18(a) and (b) for Unit-3 output voltage and current) confirms the stable operation even after islanding operation.

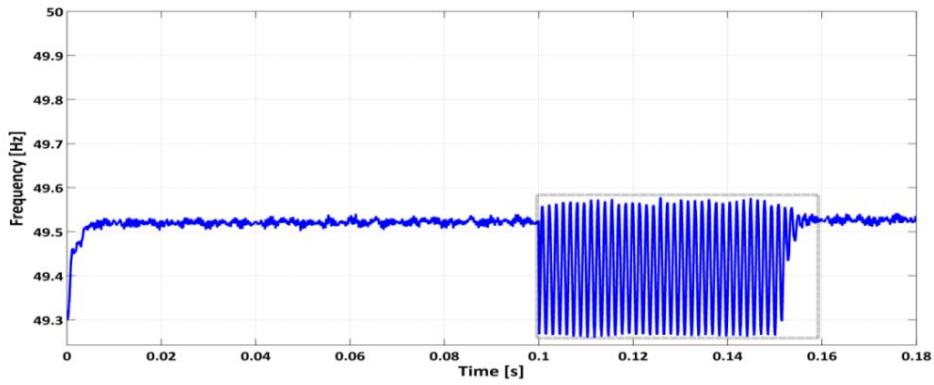


(a)

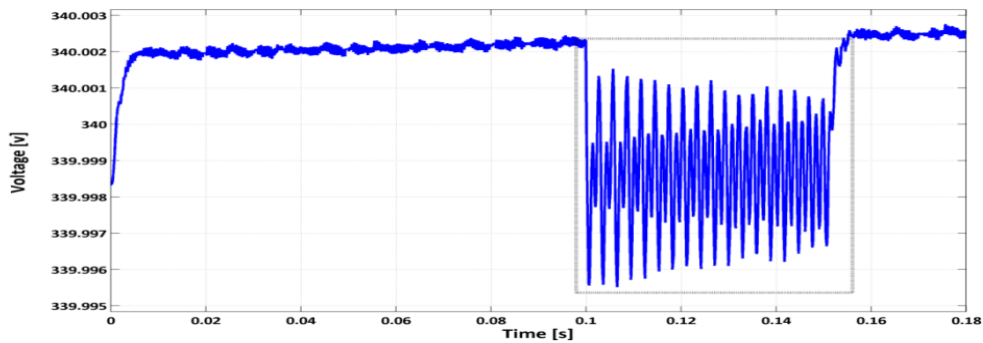


(b)

Fig. 13. a) Operating frequency; b) operating voltage of adaptive droop control based Unit-2 under L-G fault.

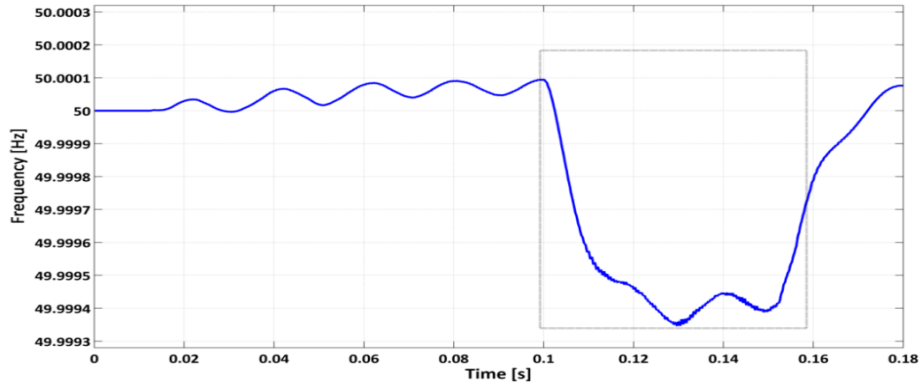


(a)

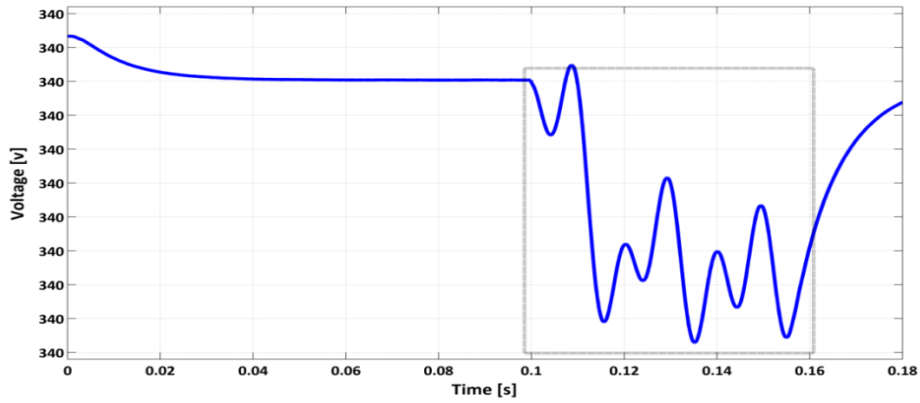


(b)

Fig. 14. a) Operating frequency; b) operating voltage of traditional droop control based Unit-3 under L-L fault.

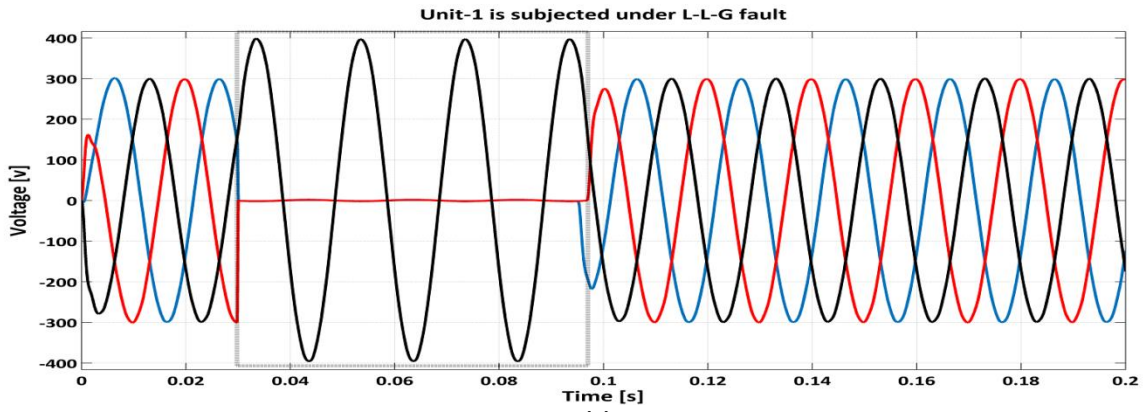


(a)

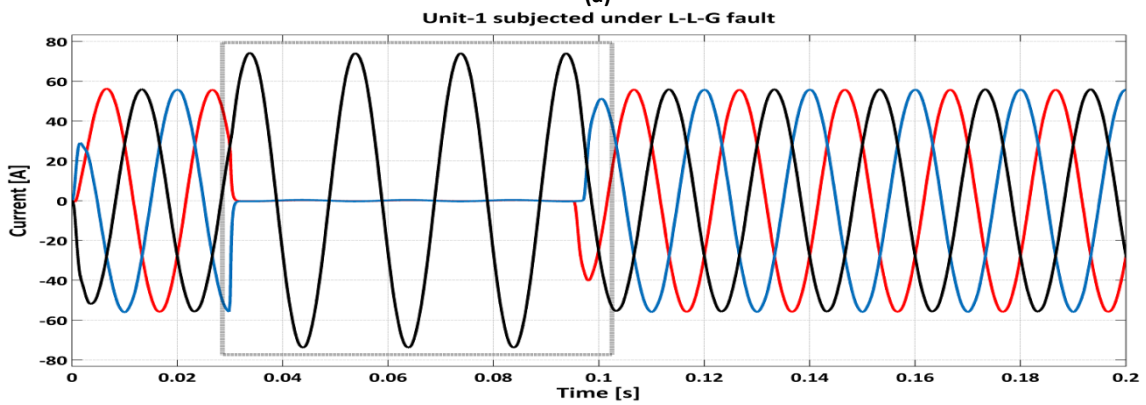


(b)

Fig. 15. a) Operating frequency; b) operating voltage of adaptive droop control based Unit-3 under L-L fault.



(a)



(b)

Fig. 16. Output voltage of: a) Unit-1 under L-L-G fault; b) Unit-2 under L-L-G fault.

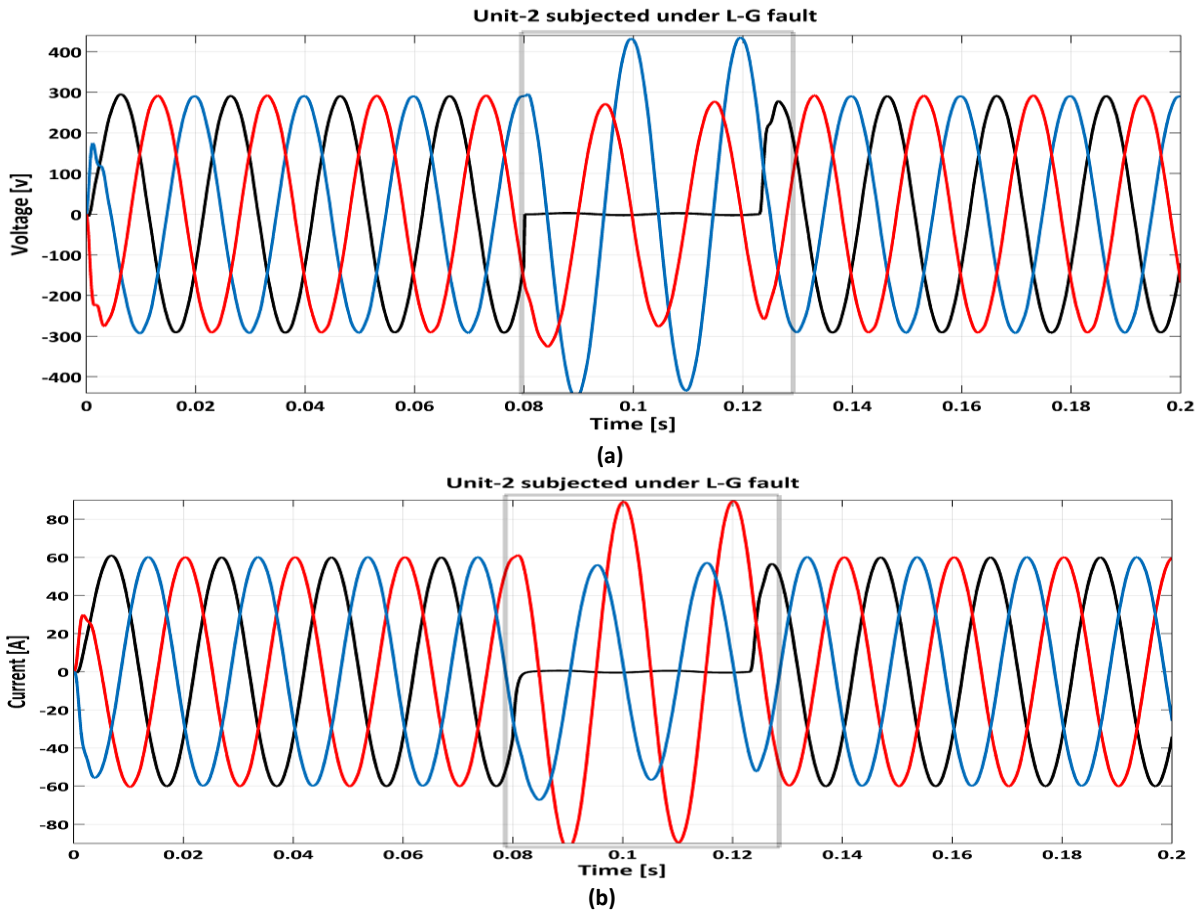


Fig. 17. a) Output voltage; b) output current of Unit-2 under L-G fault.

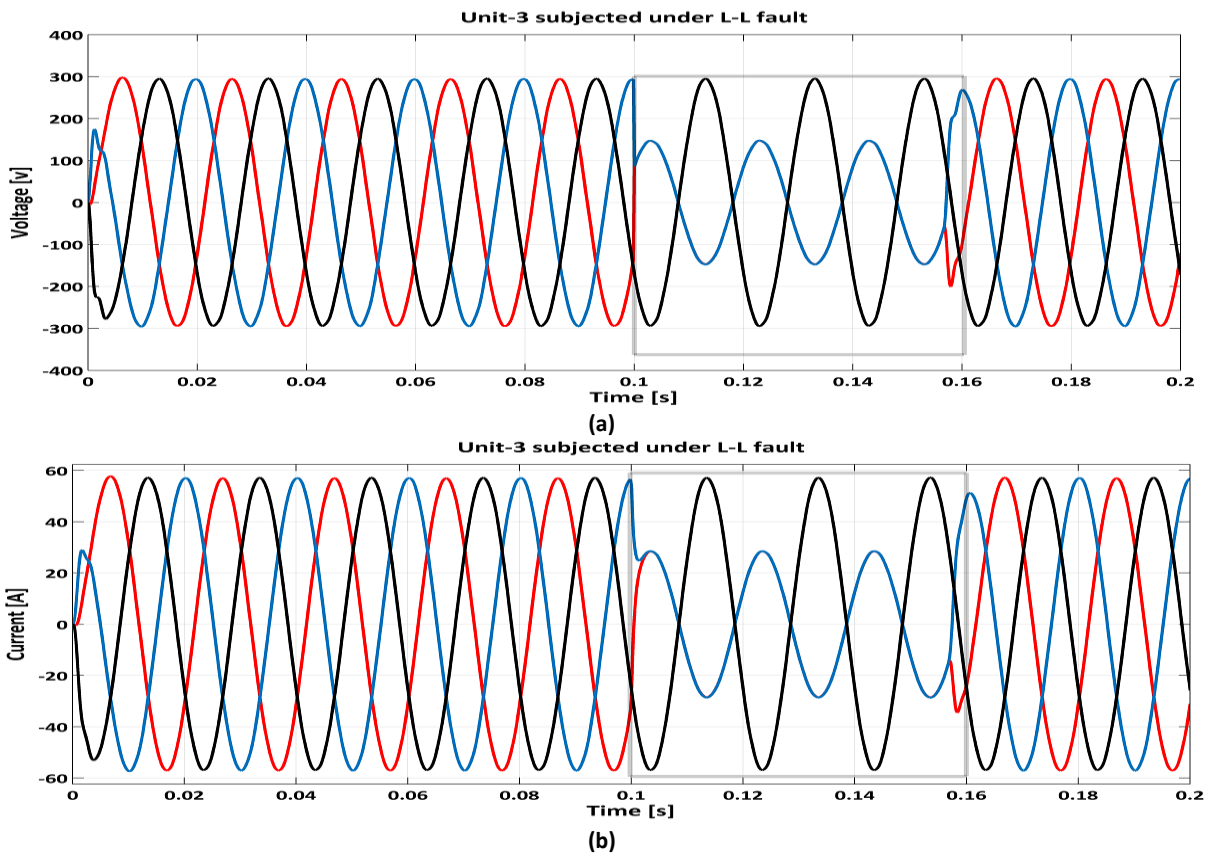


Fig. 18. a) Output voltage; b) output current of Unit-3 under L-L fault.

### 6.1.2. Symmetrical Faults

In this section, symmetrical L-L-L fault is considered to occur outside the VPP model. During this test (according to Fig. 9(b)) the solid state relay driven static switches perform complete isolation of the VPP from the utility grid in order to restrict the propagation of fault current inside the VPP. Thus, the power contribution from VPP (between 0.14 to 0.18 s according to Figs. 19(a) and (b)) becomes zero during this interval.

The voltage and frequency regulation responses during this islanded period are presented in Figs. 20 and 21. It is clearly visible in Figs. 20(a) and (b) that the oscillation of voltage and frequency is significantly large in case of traditional fixed gain droop control method. However, comparatively less frequency and voltage oscillation is obtained under the proposed adaptive droop control method as depicted in Figs. 21(a) and (b).

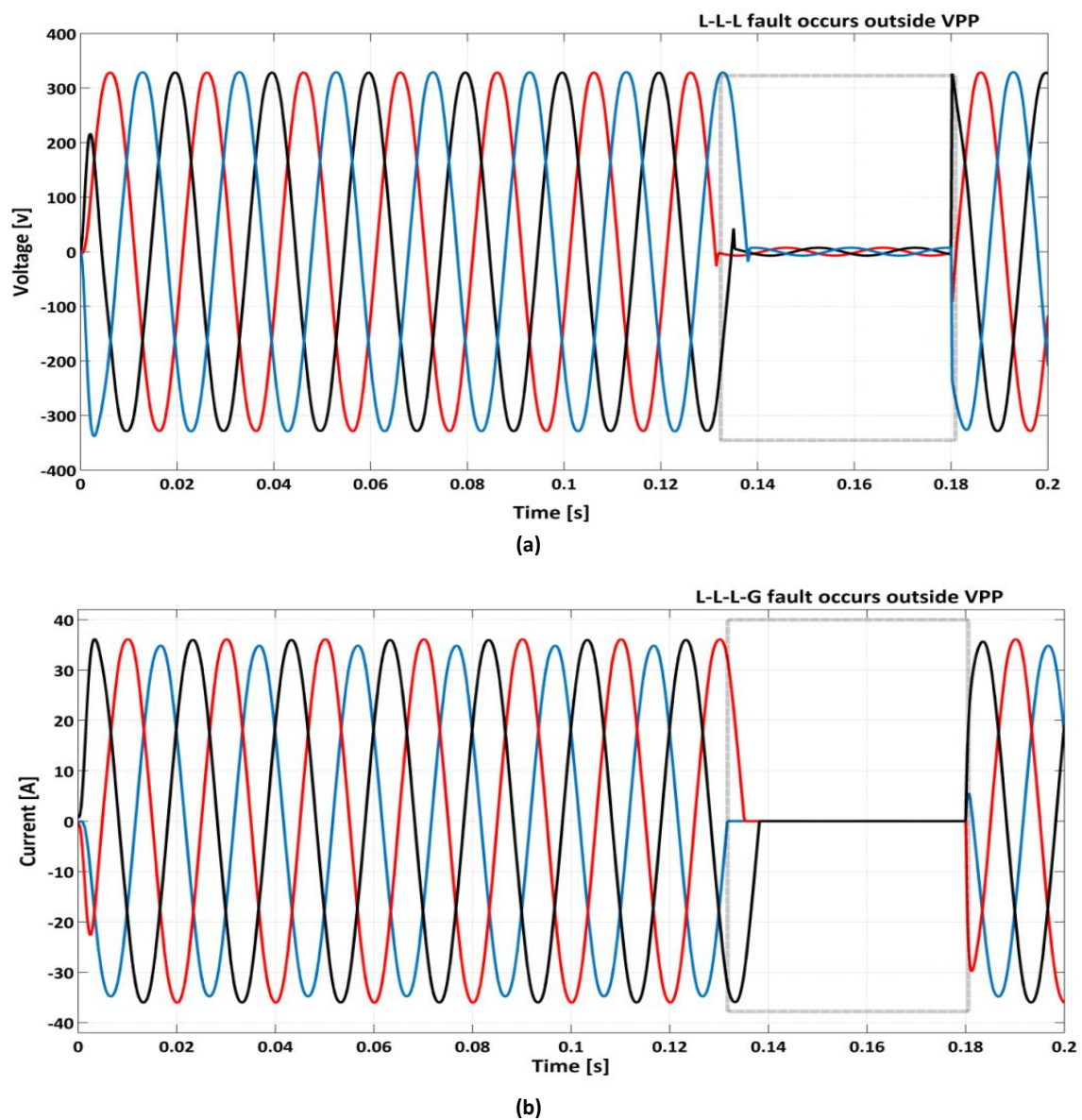
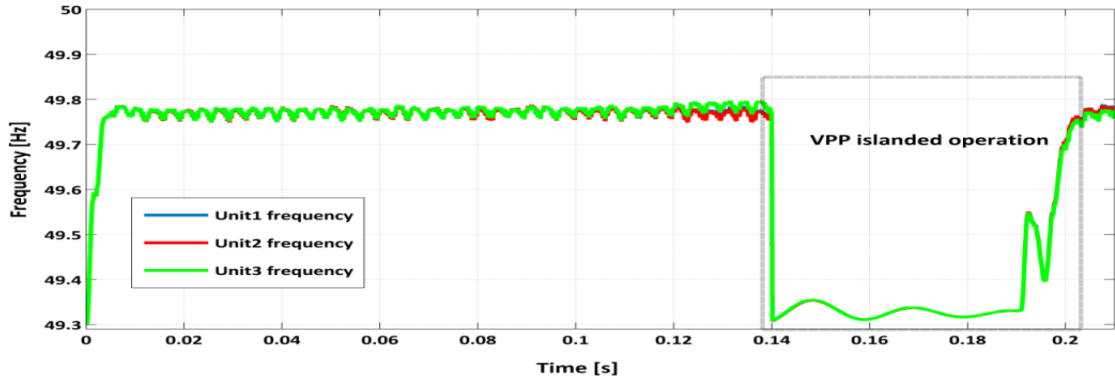
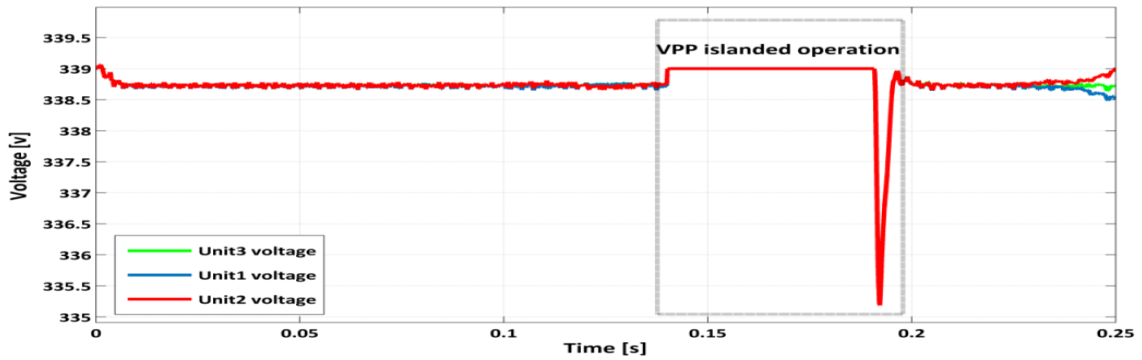


Fig. 19. a) Overall VPP Voltage response; b) current contribution from VPP to PCC.

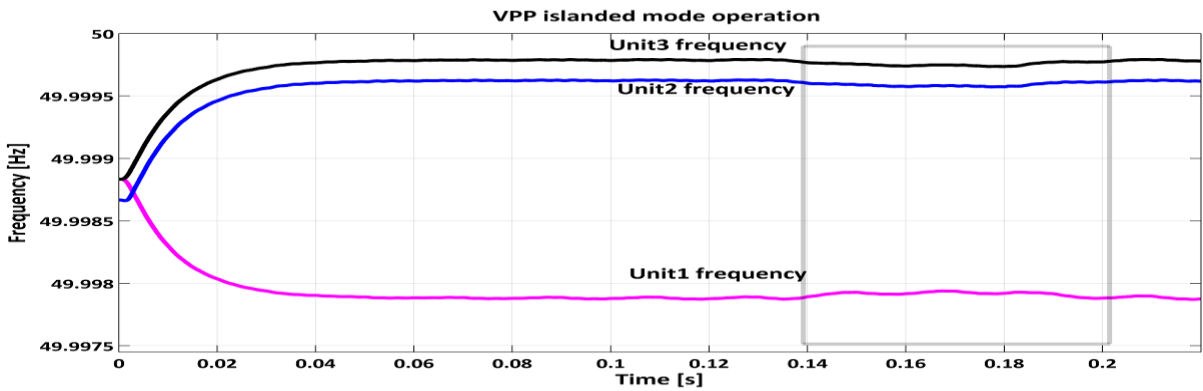


(a)

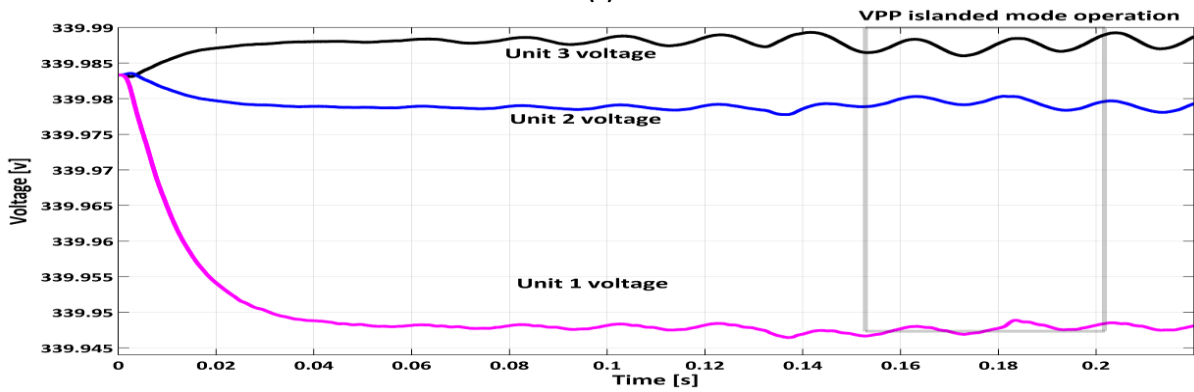


(b)

Fig. 20. a) Operating frequency; b) operating voltage of traditional droop control based three units after islanding operation.



(a)



(b)

Fig. 21. a) Operating frequency; b) operating voltage of adaptive droop control based three units after islanding operation.

## 6.2. Performance Analysis during Different Load Switching using Adaptive Droop Control Topology and Traditional Droop Control Method

So far, different faults are tested inside and outside of the considered VPP. Further, the same VPP model is tested under switching of different loads (like inductive loads, induction motors, and nonlinear loads) to examine the proposed adaptive controller performance over the traditional droop controller. Thus, at the instant of 0.18 s and 0.22 s according to Fig. 9(b), two inductive loads of different ratings are switched at PCC. Further, an induction motor at an instant of 0.24 s and a nonlinear load at an instant of 0.26 s are switched simultaneously at the PCC. According to Figs. 22(a) and (b) satisfactory system performance, in terms of limited frequency and voltage oscillations is achieved under the proposed adaptive droop controller.

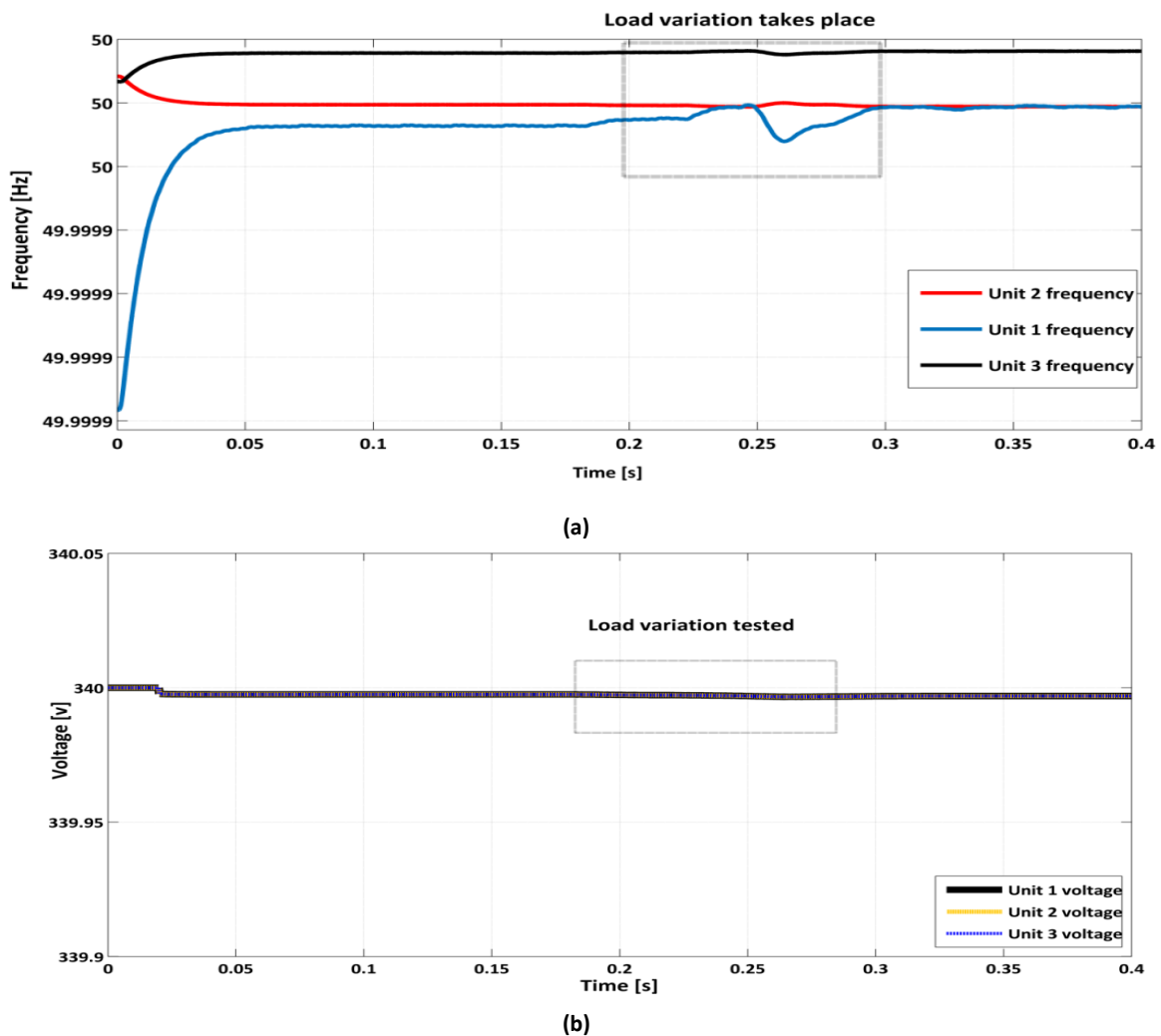


Fig. 22. a) Operating frequency; b) operating voltage of adaptive droop control based three units after islanding operation.

However, VPP with traditional fixed gain droop control topology experiences sustained voltage and frequency oscillations (according to Figs. 23(a) and (b)) during the switching of the induction motor and nonlinear load. Thus, it can be stated that much-improved frequency and voltage regulation can be achieved by utilizing the proposed adaptive droop control topology in order to ensure stable operation during sensitive load switching under the VPP scenario.

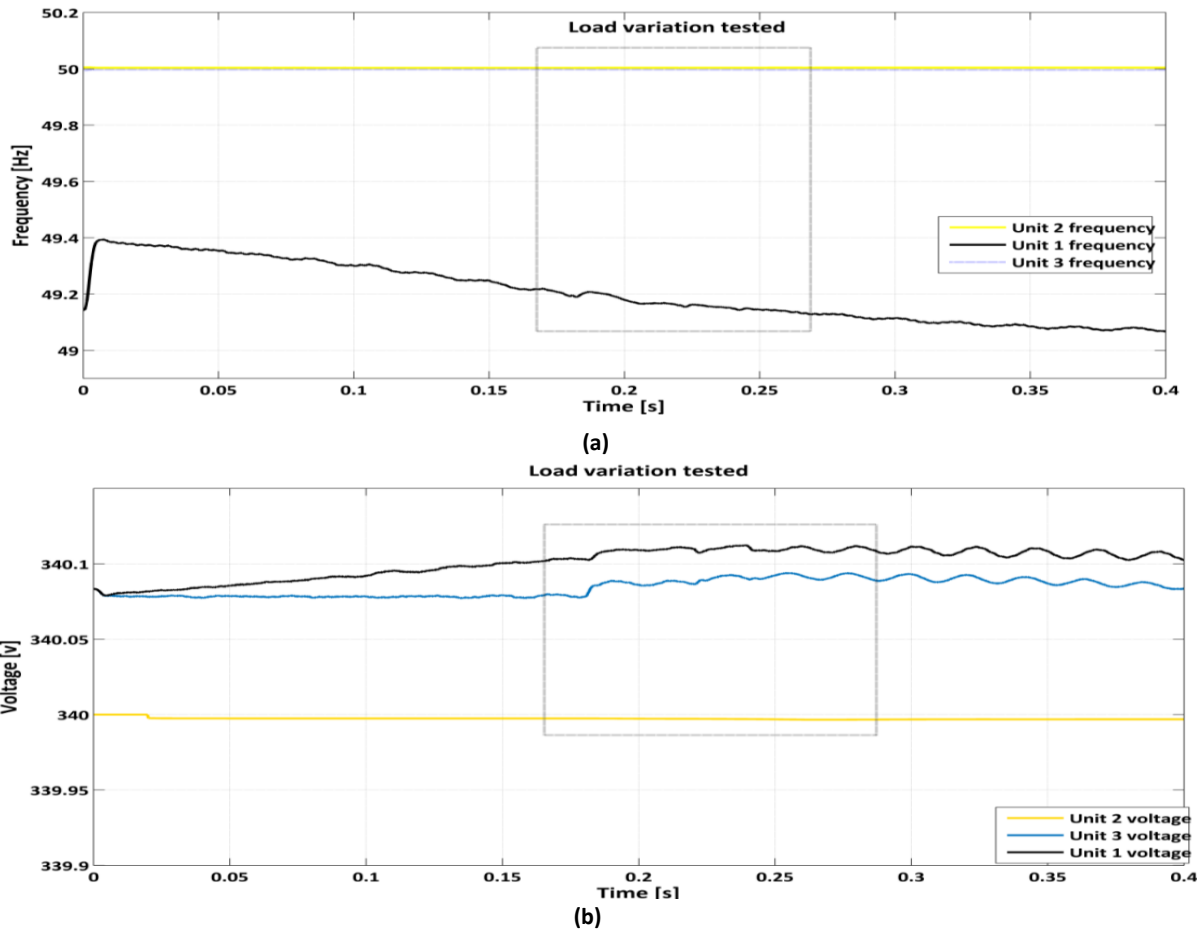


Fig. 23. a) Operating frequency; b) operating voltage of traditional droop control based three units during switching of different loads.

Table 3. Performance analysis - under different contingencies - between traditional and the proposed adaptive droop control scheme in VPP.

Simulation time [s]	Disturbance	Location of VPP	Overall VPP frequency variation [Hz]		Overall VPP voltage variation [V]	
			Traditional droop [29]	Proposed adaptive droop	Traditional droop [29]	Proposed adaptive droop
0.03-0.09	L-L-G fault	Unit 1	49-49.5 from Fig. 10(a)	49.9992-49.9998 from Fig. 11(a)	339.98-340.4 from Fig. 10(b)	340 from Fig. 11(b)
0.08-0.12	L-G fault	Unit 2	49.28-49.6 from Fig. 12(a)	49.9996-49.9999 from Fig. 13(a)	339.996-340.3 from Fig. 12(b)	340 from Fig. 13(b)
0.1-0.15	L-L fault	Unit 3	49.18-49.5 from Fig. 14(a)	49.9993-50.0001 from Fig. 15(a)	339.996-340.2 from Fig. 14(b)	340 from Fig. 15(b)
0.14-0.18	L-L-L fault	outside	-	-	-	-
0.18	Inductive load switching	PCC	49.19-50 from Fig. 23(a)	50 from Fig. 22(a)	339.9997-340.0015 from Fig. 23(b)	340 from Fig. 22(b)
0.22	Inductive load switching	PCC	49.2-50 from Fig. 23(a)	50 from Fig. 22(a)	339.999-340.11 from Fig. 23(b)	340 from Fig. 22(b)
0.24	Induction motor switching	PCC	49.2-50.0001 from Fig. 23(a)	50 from Fig. 22(a)	339.999-340.12 from Fig. 23(b)	340 from Fig. 22(b)
0.26	Non-linear load switching	PCC	49.2-50.0002 from Fig. 23(a)	50 from Fig. 22(a)	339.999-342.13 from Fig. 23(b)	340 from Fig. 22(b)

Based on the above-discussed test results, a comparative analysis between traditional fixed gain droop control and proposed adaptive droop control in the VPP scenario (considering three DER-based units) under different power system contingencies is presented in Table 3. According to Table 3, the improved frequency and voltage regulation for each test case confirms the satisfactory performance of the proposed controller over the traditional one. However, the proposed adaptive droop controller is model specific. Therefore, few controller parameters are required to modify depending upon the different power system ratings.

## 7. CONCLUSIONS

This paper introduces an adaptive droop control topology for GFM-DER based VPP in order to accomplish seamless frequency and voltage regulation under critical power system contingencies (power system faults and different load switching). Additionally, a small signal stability analysis is carried out to investigate the system performance. Based on the detailed investigation the point-wise conclusion can be furnished as follows:

- This work presents an adaptive droop control topology for GFM-DER based VPP environment. The available fixed gain droop control topology is insufficient to achieve seamless frequency and voltage regulation in VPP scenario under critical power system contingencies. In this connection, the dynamic droop gain adjustment feature of the proposed control topology overcomes the drawback of the traditional droop control scheme.
- Furthermore, an Eigenvalue-based small signal stability analysis is carried out to investigate the proposed system performance. In this scenario, utilizing the Eigenvalue analysis, a stable operating range of the proposed adaptive droop controller coefficients as well as PI controller (of the outer voltage and inner current loop) gain parameters are evaluated separately.
- Based on the obtained simulation results, it is ensured that improved transient and steady state response is achieved when the adaptive droop controller is operated within the evaluated range. Further, stable and secure system performance is achieved by utilizing the PI controllers. Based on the obtained operating range, the proper tuning of the PI controller gain parameter is further accomplished by utilizing the PSO algorithm.
- Finally, the dynamic performance analysis of the VPP has been carried out in presence of the proposed controller considering various contingencies under MATLAB/Simulink environment. In this regard, a comparative performance analysis between the proposed adaptive droop control method and the traditional fixed gain droop control method under different power system contingencies is presented. The simulation test results establish the superior performance of adaptive droop controllers over traditional droop controllers in order to regulate frequency below 1% and voltage below 5% according to IEEE 1547 standards.

In future, the proposed adaptive droop control scheme will be tested in large capacity decentralized VPP scenario in order to improve system performance in terms of voltage and frequency regulation under various power system contingencies.

## REFERENCES

- [1] S. Ogbikaya, M. Iqbal, "Reduced order model of a microgrid system for a university community in Nigeria," *Jordan Journal of Electrical Engineering*, vol. 8, no. 3, pp. 266-278, 2022.
- [2] M. Hosseinpour, T. Sabetfar, A. Dejamkhooy, "Power conditioner design and control for a grid-connected proton exchange membrane fuel cell," *Jordan Journal of Electrical Engineering*, vol. 9, no. 1, pp. 98-124, 2023.
- [3] M. Shafiekhani, A. Ahmadi, O. Homaei, M. Shafie-khah, J. Catalao, "Optimal bidding strategy of a renewable-based virtual power plant including wind and solar units and dispatchable loads," *Energy*, vol. 239, pp. 122379, 2022.
- [4] S. Sadeghi, H. Jahangir, B. Vatandoust, M. Golkar, A. Ahmadian, A. Elkamel, "Optimal bidding strategy of a virtual power plant in day-ahead energy and frequency regulation markets: a deep learning-based approach," *International Journal of Electrical Power and Energy Systems*, vol. 127, pp. 106646, 2021.
- [5] S. Yin, Q. Ai, Z. Li, Y. Zhang, T. Lu, "Energy management for aggregate prosumers in a virtual power plant: a robust Stackelberg game approach," *International Journal of Electrical Power and Energy Systems*, vol. 117, pp. 105605, 2020.
- [6] W. Guo, P. Liu, X. Shu, "Optimal dispatching of electric-thermal interconnected virtual power plant considering market trading mechanism," *Journal of Cleaner Production*, vol. 279, pp. 123446, 2021.
- [7] K. Zuo, L. Wu, "A review of decentralized and distributed control approaches for islanded microgrids: novel designs, current trends, and emerging challenges," *The Electricity Journal*, vol. 35, no. 5, pp. 107138, 2022.
- [8] B. Alghamdi, C. Cañizares, "Frequency regulation in isolated microgrids through optimal droop gain and voltage control," *IEEE Transactions on Smart Grid*, vol. 12, no. 2, pp. 988-998, 2020.
- [9] A. Bintoudi, L. Zyglakis, A. Tsolakis, D. Ioannidis, L. Hadjidemetriou, L. Zacharia, N. Al-Mutlaq, M. Al-Hashem, S. Al-Agtash, E. Kyriakides, C. Demoulias, "Hybrid multi-agent-based adaptive control scheme for AC microgrids with increased fault-tolerance needs," *IET Renewable Power Generation*, vol. 14, no. 1, pp. 13-26, 2020.
- [10] X. Lu, S. Xia, G. Sun, J. Hu, W. Zou, Q. Zhou, M. Shahidehpour, K. Chan, "Hierarchical distributed control approach for multiple on-site DERs coordinated operation in microgrid," *International Journal of Electrical Power and Energy Systems*, vol. 129, pp. 106864, 2021.
- [11] F. Jamshidi, M. Salehizadeh, F. Gholami, M. Shafie-khah, "An optimal approach for load-frequency control of islanded microgrids based on nonlinear model," *Optimization, Learning, and Control for Interdependent Complex Networks*, pp. 257-275, 2020.
- [12] P. Ge, Y. Zhu, T. Green, F. Teng, "Resilient secondary voltage control of islanded microgrids: an eskbf-based distributed fast terminal sliding mode control approach," *IEEE Transactions on Power Systems*, vol. 36, no. 2, pp. 1059-1070, 2020.
- [13] J. Schiffer, T. Seel, J. Raisch, T. Sezi, "Voltage stability and reactive power sharing in inverter-based microgrids with consensus-based distributed voltage control," *IEEE Transactions on Control Systems Technology*, vol. 24, no. 1, pp. 96-109, 2015.
- [14] Z. Ma, Q. Zhang, Z. Wang, "Safe and stable secondary voltage control of microgrids based on explicit neural networks," *IEEE Transactions on Smart Grid*, 2023.
- [15] W. Xing, H. Wang, L. Lu, S. Wang, M. Ouyang, "An adaptive droop control for distributed battery energy storage systems in microgrids with DAB converters," *International Journal of Electrical Power and Energy Systems*, vol. 130, pp. 106944, 2021.
- [16] S. Ferahtia, A. Djeroui, H. Rezk, A. Chouder, A. Houari, M. Machmoum, "Adaptive droop based control strategy for DC microgrid including multiple batteries energy storage systems," *Journal of Energy Storage*, vol. 48, pp. 103983, 2022.

- [17] W. Yao, Y. Wang, Y. Xu, C. Dong, "Small-signal stability analysis and lead-lag compensation control for DC networked- microgrid under multiple time delays," *IEEE Transactions on Power Systems*, vol. 38, no. 1, pp. 921–933, 2022.
- [18] B. Alghamdi, C. Cañizares, "Frequency regulation in isolated microgrids through optimal droop gain and voltage control," *IEEE Transactions on Smart Grid*, vol. 12, no. 2, pp. 988–998, 2020.
- [19] M. Dokus, F. Stallmann, A. Mertens, "Sequence impedance-based stability analysis of AC microgrids controlled by virtual synchronous generator control methods," *IFAC-Papers on Line*, vol. 53, no. 2, pp. 12221–12228, 2020.
- [20] L. Zhang, H. Zheng, Q. Hu, B. Su, L. Lyu, "An adaptive droop control strategy for islanded microgrid based on improved particle swarm optimization," *IEEE Access*, vol. 8, pp. 3579–3593, 2019.
- [21] J. Vega-Herrera, C. Rahmann, F. Valencia, K. Strunz, "Analysis and application of quasi-static and dynamic phasor calculus for stability assessment of integrated power electric and electronic systems," *IEEE Transactions on Power Systems*, vol. 36, no. 3, pp. 1750–1760, 2020.
- [22] F. Sanchez Gorostiza, F. Gonzalez-Longatt, "Optimised TSO-DSO interaction in unbalanced networks through frequency responsive EV clusters in virtual power plants," *IET Generation, Transmission and Distribution*, vol. 14, no. 21, pp. 4908–4917, 2020.
- [23] N. Nasser, M. Fazeli, "Buffered-microgrid structure for future power networks; a seamless microgrid control," *IEEE Transactions on Smart Grid*, vol. 12, no. 1, pp. 131–140, 2020.
- [24] L. Ahmethodzic, M. Music, "Comprehensive review of trends in microgrid control," *Renewable Energy Focus*, vol. 38, pp. 84–96, 2021.
- [25] A. Paspatis, G. Konstantopoulos, S. Dedeoglu, "Control design and small-Signal stability analysis of inverter-Based microgrids with inherent current limitation under extreme load conditions," *Electric Power Systems Research*, vol. 193, pp. 106929, 2021.
- [26] S. Leitner, M. Yazdani, A. Mehrizi-Sani, A. Muetze, "Small-signal stability analysis of an inverter-based microgrid with internal model-based controllers," *IEEE Transactions on Smart Grid*, vol. 9, no. 5, pp. 5393–5402, 2017.
- [27] Y. Han, M. Yang, P. Yang, L. Xu, X. Fang, K. Zhang, F. Blaabjerg, "Reduced-order model for dynamic stability analysis of single-phase islanded microgrid with BPF-based droop control scheme," *IEEE Access*, vol. 7, pp. 157859–157872, 2019.
- [28] N. Patel, A. Kumar, N. Gupta, S. Ray, B. Babu, "Optimised PI-4VPI current controller for three-phase grid-integrated photovoltaic inverter under grid voltage distortions," *IET Renewable Power Generation*, vol. 14, no. 5, pp. 779–792, 2020.
- [29] S. Shrivastava, B. Subudhi, S. Das, "Distributed voltage and frequency synchronisation control scheme for islanded inverter-based microgrid," *IET Smart Grid*, vol. 1, no. 2, pp. 48–56, 2018.